Title

Homeostasis of a representational map in the neocortex

Authors & Affiliations

Takahiro Noda[1], Eike Kienle[1], Jens-Bastian Eppler[2], Dominik F. Aschauer[1], Matthias Kaschube[2], Yonatan Loewenstein[3], and Simon Rumpel[1]

1: Institute of Physiology, Focus Program Translational Neurosciences, University Medical Center, Johannes Gutenberg University-Mainz, Mainz, Germany

2: Frankfurt Institute for Advanced Studies and Institute for Computer Science, Goethe University Frankfurt, Frankfurt, Germany

3: Department of Neurobiology, the Federmann Center for the Study of Rationality and the Edmond and Lily Safra Center for Brain Sciences, The Hebrew University, Jerusalem, Israel

Summary

Cortical function and the processing of sensory stimuli is remarkably robust against the continuous loss of neurons during aging, but also accelerated loss during prodromal stages of neurodegeneration[1,2]. Population activity of neurons in sensory cortices builds a representation of the environment in form of a map that is structured in an informative way for guiding behavior. Here, we used the mouse auditory cortex as a model and probed the robustness of a representational map against the removal functionally characterized neurons. Specifically, we tested in how far the structure of the representational map is safeguarded by homeostatic network mechanisms. We combined longitudinal two-photon calcium imaging of population responses evoked by a diverse set of sound stimuli in the mouse auditory cortex with a targeted microablation of individual, functionally characterized neurons. Unilateral microablation of 30 - 40 selected sound-responsive layer 2/3 neurons led to a temporary collapse of the representational map that showed a subsequent recovery. At the level of individual neurons, we observed that the recovery was predominantly driven by neurons that were unresponsive to the sounds before microablation and gained responsiveness during the time course of several days. The remodeling of the spared network was mediated by a shift of the distribution of tuning curves towards the ablated neurons and was accompanied by a shift in the excitation/inhibition balance. Together, our findings provide a link between the plasticity of individual neurons and the population dynamics of sensory representations mediating robustness of cortical function. The dynamic reconstitution of the structure of activity patterns evoked by sensory stimuli despite a permanent loss of neurons in the network demonstrates a homeostatic maintenance of sensory representations in the neocortex.

Introduction

Sensory information is represented in the cortex in form of a representational map in which various properties of sensory entities are encoded as similarity or dissimilarity of neuronal activity patterns[3,4]. The representational map offers a general framework to describe neuronal population activity along a sensory-motor transformation, whereas in sensory areas of the cortex perceptual aspects of the stimuli dominate the structure of the map. Practically, the structure of a representational map can be experimentally characterized by a similarity measure between population responses to different sensory stimuli[5] and has been utilized as a readout of neuronal function in various sensory domains to characterize perception-related behavior[6-9], including the auditory modality[10,11].

After emergence during an individual's development, the stability of a representational map is continuously challenged during adulthood. At the level of sensory evoked activity, a continuous reformatting of tuning properties of individual neurons has been described in recent year as representational drift. Such a continuous drop in and drop out of individual neurons from the population response demonstrated in various brain regions[8,11-14]. A possible mechanism for these functional changes in tuning lies in substantial plastic changes in the synaptic structure of neocortical circuits that can be observed under environmentally and behavioral stable conditions[15-22].

Apart from changes in the connectivity structure, also the loss of neurons, i.e., nodes in the network, challenge the stability of representational maps. Given that the brain is largely postmitotic, a continuous loss of neurons has been observed during aging[23-26]. In the context of neurodegenerative diseases this loss is substantially increased. Surprisingly, however, during healthy aging as well as even advanced prodromal neurodegenerative stages, a remarkable robustness in cognitive functions has been described until a tipping point has been reached[1,2,27].

What processes could endow cortical networks with robustness against these challenges? On the one hand, specific activity patterns could rely on a highly redundant connectivity structure, such that substantial changes in the network do not alter activity patterns[28-30]. On the other hand, specific manipulations on a small number of neurons can nevertheless have a big effect on activity patterns and behavior[31-34]. This hints that neuronal activity patterns may not be intrinsically robust, but are stabilized by dynamic feedback mechanisms.

In the body various important physiological parameters such as blood pressure or body temperature are challenged by various short- and long-term disturbances, but kept within a functional range due to homeostatic regulation[35]. In neural systems, few examples of homeostasis have been demonstrated, including firing rate homeostasis at the level of individual neurons[36-38] and network homeostasis of pacemaker patterns in the gastropyloric ganglion in crayfish[39]. In how far homeostatic mechanisms also play a role in protecting higher-order brain functions in the cortex is less well understood, as classic schemes for homeostatic controller[40,41] with firing rate as a regulatory valuable are insufficient to explain homeostatic behaviors at different network scales[42]. In order to test in how far homeostatic mechanisms safeguard a cortical circuit mediating sensory perception, we here probed the robustness of a representational map against the experimentally induced loss of functionally selected neurons.

Results

Long-term stability of a representational map despite volatility in single-cell tuning

To monitor the long-term dynamics of auditory representations in the mouse auditory cortex, we co-injected two recombinant adeno-associated virus vectors to express the genetically encoded calcium indicator, GCaMP6m as a neuronal activity marker[43] and the fusion protein, H2B::mCherry to highlight the nuclei of transduced neurons for high-fidelity image registration and analysis (Fig. 1a,b, see Methods)[11,44]. We performed intrinsic signal imaging in response to a set of pure-tone stimuli with different frequencies to functionally identify the tonotopic structure of the auditory cortex to guide subsequent two-photon imaging (Extended Data Fig. 1a). For calcium imaging experiments in awake, head-fixed, passively listening mice, we used a stimulus set of brief (50 – 70 ms) sounds consisting of 19 sinusoidal pure tones (PT) and 15 complex sounds (CS) characterized by temporally modulated power in multiple frequency bands (34 stimuli in total, 10 repetitions each, presented in a pseudorandom order, Fig. 1c) delivered in free field[11] using a calibrated speaker at 70 dB sound pressure level. Mice were habituated to head fixation and pre-exposed to the set of sound stimuli for at least one week to perform imaging in familiar behavioral and experimental conditions [11,45]. In a given mouse, we consecutively imaged neuronal activities in 6-8 Fields Of Views (FOVs) vertically aligned within layer 2/3 (Extended Data Fig. 1b). When assessing the trial-averaged calcium responses to the set of sound stimuli in a FOV (~140 - 180 neurons), we observed diverse tuning (Fig. 1c) in a smaller fraction of neurons (~10 - 14%), whereas the majority of neurons were unresponsive in a given imaging session. The neuronal populations were tracked and re-imaged for 6 time points at a 2-day interval and a last imaging time point after a 4-day interval (9,451 neurons, 59 FOVs, 9 mice; Extended Data Fig. 1c).

Consistent with previous reports[11,46], we observed a substantial change in responsiveness and tuning in individual neurons during the time course of the experiment in our dataset. Whereas the tuning curves of neurons categorized as responsive to any of the 34 stimuli on imaging day -1 tiled the set of stimuli, the representation substantially became sparse when considering the responses in the same set of neurons to the same stimuli on earlier or later imaging time points (Fig. 1d). To quantify the changes in tuning, we calculated the Pearson correlation of pairs of tuning curves that were constructed by averaging the responses from a randomly chosen half of the trials. For day -1 all trials were recorded on that day, for the other intervals, one half of the trials stemmed from day -1 and the other half from the other imaging days. The correlation of tuning curves showed a monotonous and symmetric decay from imaging day -1 to increasing intervals (Fig. 1e, One-way ANOVA across days, $F(6,56) = 7.77$, $p = 4.21\times10^{-6}$; correlation between day -3 and day +1, between day -5 and day +3, paired t-test $p = 0.69$, $p = 0.12$, respectively).

The volatility in tuning of individual neurons, however, was balanced at the population level. When identifying the neurons that were significantly responsive on a given day, their number was comparable throughout the experiment and their sorted response profiles were highly similar across days (Fig. 1f and Extended Data Fig. 1d). Also, the Pearson correlation of average tuning curves from the halves of trials obtained on a given day was largely constant, indicating a stable level of trial-to-trial reliability of responses (Fig. 1g, One-way ANOVA, $F(6,56)=0.55$, $p = 0.77$). Similarly, the ability to decode the identity of a pair of sound stimuli from neural population activity gradually decreased when single-trial neural activity patterns were tested at increasing intervals from the day when activity patterns were recorded to train the classifier. However, when the decoder was trained and tested with activity patterns recorded at the same day, the performance was largely stable across imaging days (Extended Data Fig. 1 e).

We next assessed how sounds were represented at the population-level in the form of a representational map using an approach analogous to a Representational Similarity Analysis (RSA)[5]. In a given FOV, we created single-trial response vectors by averaging the amplitude of the calcium signals for each neuron within a 400ms time window after each sound presentation. We constructed a similarity matrix by calculating the average Pearson correlation of the response vectors for all pairwise combinations of trials evoked by the same stimulus for the elements along the diagonal and for all combinations of response vectors from a given pair of stimuli for the off-diagonal elements [11]. To obtain a global measure of pairwise similarity of the population responses, we averaged the similarity matrices of all FOVs for each day (Fig. 1h). The resulting grand-averaged similarity matrix of the neuronal activity patterns evoked by the set of sound stimuli provides a pairwise measure of perceptual similarity in mice allowing to predict the level of generalization in various behavioral paradigms (Extended Data Fig. 2) [10,11]. Therefore, the similarity matrix, or its two-dimensional display constructed by PCA (Fig. 1j), provides a useful estimate of the internal representational map reflecting behaviorally relevant relational information of sounds.

Over the time course of the experiment, the structure of the similarity matrices (Fig. 1h), the average correlation in the matrices along the diagonal and off-diagonal (Fig. 1i) and the corresponding 2D-displays showed a remarkably high level of similarity. This indicated that the pairwise representational similarity or dissimilarity of the various pairs of sounds is largely preserved despite the substantial drop-in and drop-out of individual neurons from the population response (Fig. 1d). Also, at the level of population response vectors, we found that the average Pearson correlation of population response vectors between neighboring days was generally high, while gradually decreasing for larger intervals (Fig. 1k). Together, these observations indicated that a dynamic mechanism may maintain the global structure of the representational map despite the drift in single cell tuning and decorrelation of population response vectors over days.

Microablation of sound-responsive neurons leads to a transient collapse of the representational map

In order to reveal network mechanisms that support the maintenance of the representational map, we permanently removed individual, functionally identified neurons from the local microcircuit using targeted laser microablation[33,47,48]. We performed point scanning on the center of the nucleus of a targeted neuron using 760 nm laser wavelength with 100 - 220 mW intensity (Extended Data Fig. 3a) and monitored the fluorescence signal of the calcium indicator. The procedure was applied for several seconds until an abrupt elevation of the signal was observed (see Methods, Extended Data Fig. 3b). Typically, the calcium signal remained increased for the rest of the imaging session (Extended Data Fig. 3c-d), but after two days, both the calcium signal and the H2B::mCherry label of the nucleus was no longer detectable (Fig. 2a).

In a pilot experiment characterizing the ablation procedure (2 mice, 111 targeted neurons), we found that a removal of individual neurons was achieved in the majority of cases (76.6%), whereas only in a minority of cases the procedure was unsuccessful (13.5%) or lead to an unspecific damage also in neurons nearby to the targeted neuron (9.9%) (Fig. 2b, Extended Data Fig. 3c-d). Furthermore, we evaluated the effect of microablation by re-identifying individual targeted cells in fixed brain sections counter stained by DAPI. We found that the categorization of successfully ablated cells based on the permanent loss of the nuclear marker in vivo was tightly correlated with a complete loss or abnormally fragmented morphology of the nucleus in the fixed brain sections (Extended Data Fig. 3e-i).

After observing that the structure of the representational map is stably maintained despite substantial turnover of the responsiveness in individual neurons, we now tested the robustness against the permanent loss of specific, functionally identified neurons. We first derived a distribution of sound-evoked response amplitudes across neurons in each FOV during baseline considering day -3 and day -1 before the day of microablation (day 0) (Fig. 2 c) (see methods). We devised two cohorts of mice, one in which particularly sound-responsive neurons were targeted for microablation (10 mice), and a second cohort in which non-sound responsive neurons were targeted (10 mice). In each cohort 3-7 neurons were microablated per FOV resulting in a largely uniform distribution along cortical depth within layer 2/3. In total, we microablated on average 34.1 ± 2.81 cells per mouse in the sound-responsive cohort and 35.3 ± 2.37 cells per mouse in the non-sound responsive cohort, which corresponded to ~3% of imaged and analyzed neurons (Extended Data Fig. 4a-c). For the further analysis of sound-evoked patterns during baseline and the time points after microablation, we excluded the actually microablated cells in the sound responsive and non-sound responsive cohort. In addition, we excluded a comparable number of neurons with similarly large responses and low responses of the distribution of sound-evoked response amplitudes ("high category neurons" and "low category neurons", respectively) for analysis, that corresponded to the ablated cells in the other cohorts (Fig. 2 c). In the end, we considered 10,078 cells in 69 FOVs in the sound-responsive cohort, 10,604 cells in 73 FOVs in the non-sound responsive cohort and 8,878 cells in 59 FOVs in the control group allowing us to focus our analysis on the effects of microablation in the part of the neuronal network that was not directly targeted and to provide an unbiased comparison of sound-evoked responses between the different experimental cohorts (Extended Data Fig. 4d-k).

To assess the sensitivity of the representational map against the loss of a few tens of neurons, we again constructed averaged similarity matrices and corresponding 2D-displays for each time point throughout the experiment. During baseline, we observed a largely stable structure of the representational map in the sound-responsive cohort as well as in the non-sound responsive cohort, that was similar to the control group shown in Fig. 1h, j. Remarkably, in the cohort where particularly sound responsive neurons were microablated, we observed that the map had collapsed on the day after microablation, but showed a recovery during subsequent days regaining a structure that was again comparable to the one observed during baseline (Fig. 2d-f; Two-sample t-test of normalized average correlation between baseline days vs. day +1, in diagonal elements: $p = 0.011$; in off-diagonal elements: $p = 5.16 \times 10^{-6}$; One-way ANOVA of normalized average correlation across days in diagonal elements: $F(6,63) = 0.91$, $p = 0.49$; in off-diagonal elements: $F(6,63) = 2.25$, $p = 0.049$; Extended Data Fig. 5a, b). When analyzing how the representation of a pair of stimuli changed on the representational map during an imaging interval, we found that the direction of change was largely independent of the initial representational distance during baseline, but showed a strong, directed movement of representationally similar stimuli after microablation (Extended Data Fig. 5c-e). Interestingly, the analysis of similarity of the population response vectors revealed a strongly reduced Pearson correlation between vectors during baseline and the time points after recovery of the representational map, which indicates that the underlying neuronal populations forming the map differ much more than expected from the drift occurring during baseline conditions (Fig. 2g).

In contrast, in the cohort of mice in which non-sound responsive neurons were mircoablated, the structure of the representational map was largely stable throughout the experiment (Fig. 2h-j; Two-sample t-test of normalized average correlation between baseline days vs. day +1 in in diagonal elements: $p = 0.23$; in off-diagonal elements: $p = 0.49$, One-way ANOVA of normalized average correlation across days in diagonal elements: $F(6,63) = 0.68$, $p = 0.67$; in off-diagonal elements:

$F(6,63) = 0.58$, $p = 0.75$; Extended Data Fig. 5a, b) and the population response vectors showed a gradual decorrelation with time that was not affected by the microablation (Fig. 2k). In general, the dynamics at the population level were comparable to the control group, indicating that the collapse of the representational map was caused by the loss of neurons contributing to the population response before microablation.

The recovery of the representational map is supported by neurons becoming sound-responsive after microablation

We next wondered what changes at the level of individual neurons underlie the collapse and recovery of the representational map. The removal of a few tens of neurons did not lead to a significant change in the fraction of sound responsive cells in the remaining network (Fig. 3a, One-way ANOVA across days, sound responsive cohort: $F(6,63) = 1.47$, $p = 0.20$; non-sound responsive cohort: $F(6,63) = 0.80$, $p = 0.57$; control: $F(6,56) = 0.26$, $p = 0.95$) and the levels of spontaneous activity also remained largely unaffected (Extended Data Fig. 6a,b). Furthermore, the tuning width of individual neurons being responsive to pure tones or complex sounds on a given day was comparable during baseline and after microablation in the three experimental cohorts (Fig. 3b; Shape of tuning curve in b, tuning width by full-width half maximum (FWHM) over days, for sound responsive cohort, 0.41 ± 0.0097 oct (mean ± s.e.m.) in PT, 1.28 ± 0.053 stimulus indices in CS, One-way ANOVA of FWHM in PT, $F(6,63) = 0.68$, $p = 0.67$, FWHM in CS, $F(6,63) = 0.23$, $p = 0.96$; For non-sound responsive cohort, 0.44 ± 0.012 oct in PT, 1.26 ± 0.039 stimulus indices in CS, One-way ANOVA of FWHM in PT, $F(6,63) = 0.18$, $p = 0.98$, in CS, $F(6,63) = 1.38$, $p = 0.24$; For control, 0.38 ± 0.0079 oct in PT, 1.25 ± 0.046 stimulus indices in CS, One-way ANOVA of FWHM in PT, $F(6,54) = 0.32$, $p = 0.93$; in CS, $F(6,56) = 0.28$, $p = 0.94$). However, when analyzing the best response amplitude, which is the average amplitude evoked by the stimulus evoking the maximal response on a given day, we observed a delayed increase in the cohort of mice in which sound responsive neurons were microablated (Fig. 3c; One-way ANOVA for the sound responsive cohort, $F(6,63) = 6.87$, $p = 1.22\times10^{-5}$; Two-sample t-test with adjusted p-values by false discovery rate (FDR) method, on day +3, $p > 0.25$; on day +5, $p = 0.042$ between the sound responsive cohort vs. the non-sound responsive cohort; on day +9, $p = 0.013$ between the sound responsive cohort vs. control; One-way ANOVA for the non-sound responsive cohort, $F(6,63) = 2.0$, $p = 0.078$; control group, $F(6,56) = 0.66$, $p = 0.68$). In the same cohort, we also observed that the overlap of neurons showing significant sound responses on two subsequent imaging days was reduced after microablation, indicating an increase in tuning changes in individual neurons (Fig. 3d; One-way ANOVA, $F(5,54) = 6.03$, $p = 0.0002$; Two-sample t-test between change during baseline days vs. change from day -1 to day +1, $p = 9.47\times10^{-5}$; Two-sample t-test with FDR correction on day -1 → +1 between the sound responsive cohort vs. control, $p = 0.064$; the sound responsive cohort vs the non-responsive cohort, $p = 0.0165$; One-way ANOVA in the non-responsive cohort, $F(5,54) = 0.39$, $p = 0.85$; One-way ANOVA in control, $F(5,48) = 0.50$, $p = 0.78$). Consistently, we found that the ability to decode the stimulus identity from sound-evoked activity patterns was significantly decreased in the sound responsive microablation cohort when the decoder was trained on day -1 and also utilized for the other imaging days, despite the fact that decoding performance was largely stable in all experimental groups over time when training and testing was done on a given day (Extended Data Fig. 6c, d).

To further analyze the increased changes in tuning from imaging day to imaging day, we focused on the neurons categorized as sound responsive on the day before microablation and sorted them according to their tuning profile, resulting in a continuous tiling of sound responses over the 34

sound stimuli on day -1, analogous to Fig. 1d. Again, we observed that the sound responses in this set of neurons showed substantial sparsening for increasing imaging days, but this effect was more pronounced after microablation of sound responsive neurons (Fig. 3e) and similarly the tuning curves of individual neurons decorrelated faster (Fig. 3f; paired-sample t-test between day -3 vs. day +1: $p = 0.0039$ for the sound responsive cohort; Two-sample t-test between the sound responsive cohort and control on day +1: $p=0.028$; day +3: $p=0.017$; day +5: $p=0.067$; day +9: $p=0.29$). The sparsening of sound responses and the decorrelation of tuning curves in the cohort in which non-sound responsive neurons were microablated was comparable to the control group (Fig. 3g-h; paired-sample t test between day -3 vs. day +1: $p > 0.5$ for both non-responsive ablation and control; Two-sample t-test between the non-responsive cohort and control on day +1: $p = 0.54$; day +3: $p = 0.18$; day +5: $p = 0.39$; day +9: $p = 0.90$; Extended Data Fig. 6e).

The analyses of single cell response properties so far revealed that the overall responsiveness and tuning properties in the network were not strongly affected by the removal of a few tens of sound responsive neurons, but that the spared neurons participating the population response before microablation were destabilized in their responses. For the following analyses, we split our data into the neurons categorized as significantly sound responsive before microablation and the neurons with no significant sound responses on day -1, but on another imaging day, and revisited the effect of increased best response amplitudes after microablation of sound responsive neurons. We found that best response amplitudes of sound responsive neurons on day -1 were significantly reduced in the sound responsive cohort on day +1 after microablation, although a somewhat less pronounced reduction was also observed in the non-sound responsive cohort (Fig 3i, Fig3 k left, two-sample t-test between day -3 vs. day +1, for sound responsive cohort: $p = 4.54\times10^{-4}$; for non-sound responsive cohort, $p = 0.33$; for control, $p = 0.63$; Group comparison by one-sample t-test with FRA correction between sound responsive cohort vs control on day +1, $p = 0.039$; sound responsive cohort vs non-sound responsive cohort, $p = 0.096$). This loss in average response amplitude was mostly due to an increasing fraction of neurons losing responsiveness after the ablation, as the fewer neurons that stayed responsive also after microablation showed similar best response amplitudes as compared to the baseline (Extended Data Fig. 6 f).

In all three experimental cohorts some neurons that were categorized as non-responsive on a given day showed clear sound-driven responses on other days. When considering the best response amplitudes in those cells that were not responsive on the day before ablation (day -1), but responsive on any other day, we found a delayed, but substantial increase after microablation of sound-responsive neurons (Fig. 3j, Fig 3k right, One-way ANOVA across days for sound responsive cohort: $F(5,54) = 6.19$, $p = 0.0001$; for non-sound responsive cohort: $F(5,54) = 2.14$, $p = 0.075$; control: $F(5,48) = 0.45$, $p = 0.81$; Group comparison by two-sample t-test with FRA correction between sound responsive cohort vs. control on day +1, $p = 0.74$; day +3, $p = 0.14$; day +5, $p = 0.017$; day +9, $p = 0.0096$; sound responsive cohort vs. non-sound responsive cohort on day +1, $p = 0.74$; day +3, $p = 0.14$; day +5, $p = 0.017$; day +9, $p = 0.23$; non-sound responsive cohort vs. control on day +1, $p = 0.74$; day +3, $p = 0.88$; day +5, $p = 0.82$; day +9, $p = 0.068$). This indicates an increased recruitment of initially non-responsive neurons to the population response compensating for the loss of sound responsive neurons.

Next, we sought to characterize the tuning of the cells in the spared network in relationship to the tuning of microablated neurons. As a measure of similarity in tuning, we calculated the Pearson correlation of trial-averaged tuning curves constructed from the 34 sound responses from pairs of neurons. For day -1, we considered in the sound responsive cohort the tuning curves of all the neurons actually microablated on day 0 in a given mouse. In the non-sound responsive and control cohorts, we considered the set corresponding neurons with large response amplitudes (high

category neurons) on day -1 that were excluded from the analysis (Fig. 2c). For this analysis, we again separated the neurons that were responsive or non-responsive on the day before microablation. For the neurons considered responsive on day -1, we calculated for each day all pairwise combinations of pre-ablation tuning curves from the high category, independently if the spared neurons would have lost responsiveness throughout the experiment or not (Fig 3l, top row, see methods). For each day, we found a wide range of correlation coefficients stemming from similarly or dissimilarly tuned pairs of neurons, that showed a bias in the distribution towards higher values (the horizontal bars in Fig. 3l), consistent with a general preferred tuning within the vertically aligned FOVs of a given mouse. In the control cohort, relative abundance of neuron pairs with highly similar tuning gradually and symmetrically decreased for larger intervals from day -1, consistent with many of these neurons losing responsiveness (Fig. 3l, top right). When comparing the relative abundance of neuron pairs with highly similar tuning in the other cohorts, in particular the sound responsive ablation cohorts, this decrease was much more pronounced and after microablation relatively fewer cells were found that have a similar tuning as the microablated cells on day -1 (Extended Data Fig. 6g, top).

When performing the analogous analysis for the neurons categorized as non-responsive on the day before microablation, we considered those neurons in the spared network that showed a significant sound response on any other imaging day. Here, we found that the bias towards high pairwise correlations in tuning was generally less pronounced (Fig. 3l, bottom row). However, we observed that in the sound responsive ablation cohort the relative abundance of neurons with a similar tuning as the microablated neurons increased in the days after microablation as compared to the non-sound responsive ablation and control cohorts (Fig. 3l, bottom row, two-sample t-test between baseline days vs. post-ablation during day +3 - +9, in sound responsive cohort: $p = 0.028$; non-sound responsive cohort: $p = 0.29$; control: $p = 0.82$; Extended Data Fig. 6g, bottom).

In addition, we analyzed the heterogeneity in tuning observed in a given FOV using the entropy of the distribution of all significant stimulus responses from the neurons in a FOV as a quantitative measure (Extended Data Fig. 6h, i). Here, we found that for day +1 to day +9, the tuning was less diverse in the sound responsive ablation and non-sound responsive ablation cohorts when considering the neurons that were responsive on day -1. However, in the neurons gaining responsiveness during day +1 to day +9 the entropy in tuning was comparably high in the sound responsive ablation cohort (Extended Data Fig. 6i, bottom).

We wondered how far in space the microablation-induced effects on best response amplitude are propagated in the cortical network. We calculated the distribution of the average best amplitude in bins of pairwise radial distances ranging from 15 to 350 mm, such that each spared neuron contributed as many measurements as there were microablated neurons in a given mouse (Extended Data Fig. 7). Consistent with the previous analyses, we observed differential effects on best response amplitudes when splitting the neurons in those categorized as responsive on day -1 and the neurons being categorized non-responsive on day -1, but these effects were generally broad within the investigated range of distances. However, for the early days after microablation in the sound responsive ablation cohort, the increase in best amplitudes in neurons gaining responsiveness was primarily observed in nearby neurons, and seemed to propagate also for more distal neurons in the following days.

A shift in response amplitudes in excitatory and inhibitory neurons after microablation

For a subset of mice in each experimental cohort (n = 5 in sound responsive ablation; n = 5 in non-sound responsive ablation; n = 7 in control), we co-injected an AAV vector (AAV mDlx-NLS::tagBFP) labeling inhibitory cortical neurons together with the AAV vectors mediating expression of GCaMP6m and H2B::mCherry (Fig. 4a). In control experiments in a GAD67-GFP pan-interneuron reporter mouse line, we observed a highly selective expression of the mDlx control element driven blue fluorescent protein in the nuclei of neurons also co-expressing GFP (Extended Data Fig. 8a-b).

Consistent with previous studies [49-51], we observed a moderately broader tuning to pure tones as well as to complex sound stimuli in inhibitory neurons (Fig. 4b and Extended Data Fig. 8c). When calculating the fraction of neurons showing a response to the set of sounds on a given day, we did not find differences between inhibitory and excitatory neurons, generally showing a stable fraction of cells contributing to the population response (Extended Data Fig. 8d). The fraction of sound-responsive neurons was largely comparable between excitatory and inhibitory neurons, although the fraction of sound-responsive inhibitory neurons is slightly higher than that of sound-responsive excitatory neurons during baseline days (Extended Data Fig. 8d).

Similar to Fig. 3d, the overlap of neurons showing significant sound responses on two consecutive imaging days was reduced on the day after microablation of sound responsive neurons in both excitatory and inhibitory neurons (Fig. 4c, two-sided t-test between the overlap during baseline days vs. the overlap during post-ablation days for excitatory neurons: sound responsive ablation, $p = 0.0024$; non-responsive ablation, $p = 0.21$; control, $p = 0.67$; For inhibitory neurons: sound responsive ablation, $p = 7.49 \times 10^{-4}$; non-responsive ablation, $p = 0.15$; control, $p = 0.15$; For group comparison two-sided t-test with FDR adjustment in the overlap during post-ablation days, in excitatory neurons: sound responsive ablation vs. non-responsive ablation, $p = 9.11 \times 10^{-5}$; sound responsive ablation vs. control, $p = 0.003$; non-responsive ablation vs. control, $p = 0.34$; In inhibitory neurons: sound responsive ablation vs. non-responsive ablation, $p = 1.79 \times 10^{-4}$; sound responsive ablation vs. control, $p = 3.99 \times 10^{-4}$; non-responsive ablation vs. control, $p = 0.76$).

To further characterize the increased changes in tuning, we again quantified the correlation of tuning curves from day -1 to the other days for excitatory and inhibitory neurons responsive on day -1, respectively. The tuning curves of both individual excitatory and inhibitory neurons decorrelated faster after microablation of sound responsive neurons, with more pronounced decorrelation in inhibitory neurons later days (Fig. 4d, two-sampled t-test between day -3 vs. day +1, excitatory neurons: $p = 0.031$; inhibitory neurons: $p = 0.15$; Group comparison by two-sided t-test with FDR correction during post-ablation days between sound responsive cohort vs. non-sound responsive cohort, and sound responsive cohort vs. control, in excitatory neurons on day +1: $p = 0.49$, $p = 0.022$; day +3: $p > 0.5$, $p = 0.0165$; day +5: $p > 0.5$, $p = 0.132$; day +9: $p > 0.5$, $p = 0.132$; In inhibitory neurons on day +1: $p = 0.11$, $p = 0.11$; day +3: $p = 0.036$, $p = 0.015$; day +5: $p = 0.024$, $p = 0.015$; day +9: $p = 0.12$, $p = 0.16$).

Next, we investigated how response amplitudes changed in each cell type after microablation. While best response amplitudes of excitatory neurons increased after ablating sound responsive neurons (Fig. 4e top, right, One-sided t test of excitatory response against normalized reference 1 on day+1: $p=0.46$; day+3: $p=0.063$; day+5: $p=0.0031$; day+9: $p=0.0023$), best response amplitudes of inhibitory neurons decreased until day +5 (Fig. 4e bottom, right, two-sample t-test of best response amplitude between excitatory and inhibitory neurons on day +1: $p = 0.28$; day +3: $p = 0.012$; day +5: $p = 0.058$; day +9: $p = 0.65$; One-sided t-test of inhibitory response against reference 1 on day +1: $p = 0.10$; day +3: $p = 0.026$; day +5: $p = 0.18$; day +9: $p = 0.30$;) but renormalized by day+9 (baseline normalized amplitude on day +9: 1.15 ± 0.26). Response amplitudes in

inhibitory neurons were also reduced 3 to 5 days also after non-responsive ablation and remained largely constant in the control group (Fig. 4e right, Extended Data Fig. 8e-g). When again splitting neurons into two groups based on the responsiveness on day -1, the best response of both the day -1 responsive excitatory and inhibitory neurons significantly decreased after ablating sound responsive neurons with a more pronounced reduction of the amplitude in inhibitory neurons (Extended Data Fig. 8f). On the other hand, the best responses of excitatory neurons, which were unresponsive on day -1 but being responsive on the other day, substantially increased after sound responsive ablation (Extended Data Fig. 8g left) like Fig. 3k, while the best response of inhibitory neurons in the corresponding split group did not show any clear change after microablation (Extended Data Fig. 8g, right). Therefore, the balance of sound-evoked activity in the excitatory and inhibitory neuronal population, serving as an estimate of the E-I ratio, increased for both sound responsive and non-sound responsive cohorts 3 to 5 days after microablation and returned to a level comparable to that of control on day +9 (Fig. 4f, two-sided t-test with FDR adjusted p-values, sound responsive cohort vs. control, non-sound responsive cohort vs. control and sound responsive cohort vs. non-sound responsive cohort, on day +1: $p > 0.5$ for all combinations ; day +3, $p = 0.039$, $p = 0.039$, $p = 0.16$; day +5, $p = 0.045$, $p = 0.032$, $p = 0.27$; day +9: $p > 0.5$ for all combinations, respectively; normalized E-I ratio on day +9, 1.09 ± 0.088 for responsive ablation, 1.10 ± 0.11 for non-responsive ablation). We did not observe altered decay time constants of the calcium transients throughout the experiment, corroborating the idea that the changes in best response amplitudes reflect microablation-induced differences in neuronal activity, rather than alterations in the expression levels of calcium binding proteins (Extended Data Fig. 8h, i).

Delayed recovery of the representational map after selective microablation of inhibitory neurons

The vast majority of the microablated neurons in both the sound responsive cohort and the non-sound responsive cohort were putatively excitatory neurons (Extended Data Fig. 4a and 8). We therefore wondered in how far the differential effects induced by microablation in excitatory and inhibitory neurons and responsive and unresponsive neurons prior to microablation do depend on the type of neurons removed from the network. To address this, we conducted another experimental series in which we selectively targeted inhibitory neurons for microablation ($n = 6$ mice). As before, we derived a distribution of sound-evoked response amplitudes from the neurons of each FOV during baseline (day -3 and -1) (Fig. 5a) and identified the inhibitory neurons based on the mDlx-driven blue fluorescent reporter (inset in Fig. 5a). We primarily targeted sound responsive inhibitory neurons, however, given the much lower density compared to excitatory neurons (~10% of the local population, Extended Data Fig. 8a) we additionally microablated inhibitory neurons categorized as non-responsive, in order to remove in total a comparable number as in the other experimental cohorts (Extended Data Fig. 4a-c).

We found that the representational map is similarly sensitive to the removal of inhibitory neurons and we observed a collapse as previously seen in the sound responsive microablation cohort. (Fig. 5c and e, Two-sample t-test of normalized average correlation between baseline days vs. day +1, in diagonal elements: $p = 4.84\times10^{-4}$; in off-diagonal elements: $p = 7.87\times10^{-4}$). However, whereas before the structure of the map was largely comparable to baseline within three days after microablation, in the inhibitory neuron ablation cohort, the recovery seemed to be substantially delayed (Fig. 5c, d and e, One-way ANOVA of normalized average correlation across days in diagonal elements: $F(6,34) = 4.11$, $p = 0.0033$; off-diagonal elements: $F(6,34) = 2.19$, $p = 0.068$; Two-sample t-test of the average correlation during baseline vs. the average correlation during day

+3 - +9, in diagonal elements: p = 0.0011; off-diagonal elements: p = 0.043; Extended Data Fig. 5a-c). When analyzing similarity of population response vectors between days, the correlation between different days dropped after microablation of inhibitory neurons throughout the rest of the experiment, although within-the same day correlation gradually recovered later (on day +9) (Fig. 5f), indicating that population response pattern re-emerged late after inhibitory cell ablation and remained unstable from day to day.

Next, we analyzed the single-cell response properties associated with the delayed recovery in the representational map after inhibitory cell ablation. As in the sound responsive microablation cohort (Fig. 3a and b), the fraction of responsive neurons (Fig. 5g, One-way ANOVA, F(6,34) = 0.36, p = 0.90) and the shape of tuning curves were largely unaffected by inhibitory cell ablation (Fig. 5h, tuning width by FWHM over days, 0.39 ± 0.0072 oct in PT, 1.14 ± 0.049 stimulus indices in CS, One-way ANOVA of FWHM in PT, F(6,34) = 0.94, p = 0.48, FWHM in CS, F(6,34) = 1.27, p = 0.30).

Different from the sound responsive cohort, the best response amplitude did not clearly increase after microablation (Fig. 5i, One-way ANOVA across days, F(6,34) = 0.95, p = 0.47). The overlap of neurons responsive during two consecutive days after one day of inhibitory cell ablation was reduced for most days after microablation (Fig. 5j, two-sided t-test of normalized fraction of stably responsive cells between baseline days vs. day +1, p = 0.026), suggesting a similar acceleration of turnover rate in population responses after inhibitory cell ablation. Consistently, the tuning profiles of neurons sorted based on the responses on day-1 asymmetrically became sparse faster after microabtaion compared to the same time intervals during baseline days (Fig. 5k). This was also reflected in faster decorrelation in the tuning curves of individual neurons like Fig. 3f (Fig. 5l, two-sided paired t-test between day-3 and day+1, *p*=0.0064; comparison between inhibitory cell cohort vs. control by two-sided t-test on day +1, p = 0.029; day +3, p = 0.031; day +5, p = 0.15; day +9, p = 0.22).

We again split the data into neurons being categorized as responsive on day -1 before the microablation and non-responsive on day -1, but responsive on another day of the experiment. The best amplitude of neurons responsive on day-1 was again diminished on the day after microablation of inhibitory neurons (Fig. 5m left, One-way ANOVA, F(6,34) = 2.47, p = 0.043; two-sided t-test between day -3 vs. day +1, p = 0.0066, p = 0.015), but the best amplitude of neurons, which were unresponsive on day-1 did not clearly increase when inhibitory neurons were selectively microablated (Fig. 5m right, One-way ANOVA, F(5,29) = 1.28, p = 0.30).

Next, we examined the tuning of spared neurons in relation to the tuning of high category neurons including microablated neurons analogously as before. For each day, we calculated all pairwise signal correlations between tuning curves of the spared neurons responsive on day-1 and the pre-ablation tuning curves of high category neurons, which correspond to the set of neurons that were targeted in the sound responsive ablation cohort. The pairwise correlations covered a wide range between -0.6 and 1 and also showed a bias towards higher values (Fig. 5n left, horizontal bars). After inhibitory cell ablation, the relative abundance of neuron pairs with highly similar tuning showed a pronounced decrease from day -1 (Fig. 5n left and Extended Data Fig. 9d left). The neurons unresponsive on day -1 but being responsive on the other day, showed a relative overrepresentation of neurons with high pairwise correlation (Fig. 5n right and Extended Data Fig. 9 d right). Together, as observed in the sound responsive cohort, inhibitory cell ablation induced a shift of tuning in the newly responsive neurons toward the tuning of highly responsive neurons.

Whereas such a shift in tuning by newly responsive neurons was observed in both the sound responsive cohort and the inhibitory cell cohort, the change in the best response amplitude in the

corresponding neurons after microablation was only observed in the sound responsive neuron ablation cohort, suggesting that the tuning shift is unrelated to change in response amplitude, but perhaps to other properties like the shift in E-I ratio. Direct ablation of inhibitory cells caused in our experiments the strongest disbalance of E-I responses. In fact, a correlation analysis across the experimental cohorts showed that the change in E-I ratio was correlated with the bi-directional shift in tuning observed in neurons categorized responsive or unresponsive before microablation (Extended Data Fig. 10 a). The collapse and recovery of the representational map, however, was primarily correlated with the loss of best response amplitudes of the neurons responsive before microablation, and the gain of best response amplitudes of neurons categorized unresponsive before microablation, respectively (Extended Data Fig. 10 b, c). The recovery of the representational map was additionally correlated with an increase in entropy in the tuning curves observed in the neurons gaining sound responses after microablation (Extended Data Fig. 10 d).

Discussion

We used the representational map formed by the responses to a set of auditory stimuli as a readout of auditory cortex function important to mediate perception. We observed that under constant environmental and behavioral conditions, similar to reports in other brain regions[8,11-14,52-54], individual neurons show a high degree of volatility in their functional tuning properties[11]. However, not only the topographically organized frequency map along the surface of the mouse auditory cortex remains unaffected by the ongoing remodeling of tuning properties[46], but we here found that also the higher-dimensional structure of the representational map of complex sounds is stably maintained.

Despite this apparent stability, we observed that the selective removal of only a comparably small number of sound responsive neurons appears to rather selectively disrupt the correlational structure of the population responses underlying the representational map. This is surprising, given that the overall level of responsiveness to sounds (Fig. 3a) or much the basic tuning properties (Fig. 3b) of neurons in the remaining network were barely affected, even when inhibitory neurons were targeted (Extended Data Fig. 8 d). The high sensitivity suggests that the robustness of the representational map does not emerge from a highly redundant or intrinsically stable network configuration, but relies on plasticity mechanisms that constantly keep the network in a functional configuration[55,56]. While such mechanisms seem to be highly effective during basal conditions when ongoing tuning changes occur, they can be at least temporarily challenged when specific neurons are removed from the network withing short time. Selective changes in circuit function and even behavior by subtle manipulations of neuronal activity has been demonstrated previously in various contexts[31,33,34,48,57,58]. The impairment in the correlational structure of the sound responsive neurons in the remaining network may stem from the loss of co-tuned inputs from the microabalated sound responsive neurons (Fig. 3 l and Fig. 5 n)[33].

Importantly, in the sound responsive microablation cohort a largely complete recovery of the representational map was observed already after a few days, and in the inhibitory neuron microablation cohort at least a partial reconstitution occurred during the time of observation. Interestingly, the rates of turnover in responsiveness were increased following microablation of sound responsive and inhibitory neurons, and neurons gaining sound responsiveness showed comparably larger best responses already after a few days in the sound responsive microablation cohort (Fig. 3 k). This observation correlated with a shift in the balance of best response amplitudes in excitatory and inhibitory neurons, and could therefore hint to a delayed releave from inhibition. Regulation of the balance of excitation and inhibition is considered important in homeostatic

plasticity at the network level to achieve stable information transmission [59,60] and has been observed during reconfiguration of cortical circuits[61-67]. However, the increase of best response amplitudes and increase in tuning entropy in neurons gaining responsiveness after microablation was not observed in the cohort in which inhibitory neurons were microablated and the strongest shift in the E-I ratio was induced. This suggests that a simple disinhibitory scenario is not sufficient to explain the recovery of the representational map and likely multiple plasticity processes contribute[68].

Homeostasis endows various parameters in the body with robustness against diverse disturbances. Compensation of a permanent manipulation and the set back of the controlled variable to its set point, represents hallmarks of a homeostatic control circuit. In the context of our observations, the compensation of the permanent removal of neurons from a local microcircuit leading to a dynamic reorganization of the network, indicates that the correlational structure of population activity underlying a representational map is not invariably stable, but is a controlled variable underlying homeostatic regulation[39].

We speculate that the ability to compensate for the loss of microablated neurons by the selective recruitment of previously unresponsive neurons at the microcircuit level may also serve as a mechanism by which brain function may be upheld for extended periods of neuronal loss during aging and neurodegenerative disease[1,2].

Methods

rAAV cloning and production

For rAAV genome encoding for GCaMP6m under the human SynapsinI promoter, and the rAAV encoding for H2B-mCherry, two plasmids were generated as described before[11]. To elaborate the plasmid containing a gene coding the blue fluorescent protein (tagBFP), preceded with three nuclear localisation signals (3 × NLS) under the mDlx enhancer sequence (pAAV-mDlx-3NLS-tagBFP), we started from the commercially available plasmid, AAV-mDlx-NLS-mRuby2 (Addgene plasmid #99130) and a plasmid for tagBFP in our lab stock (TRE-3NLS-tagBFP, which is modified from Addgene plasmid #92202). The 3NLS-tagBFP sequence was PCR amplified from plasmid pAAV-TRE-3NLS-tagBFP. The resulting PCR product was digested with the respective enzymes and purified. From AAV-mDlx-NLS-mRuby2, NLS-mRuby2 was excised with the restriction enzyme, and the 3NLS-BFP sequence was ligated into the cut and purified. The integrity of the final plasmid pAAV-mDlx-3NLS-tagBFP was confirmed by sanger sequencing. All plasmids described above were packaged into AAV8 capsid described as previously described[69].

Mice

Experimental subjects were male C57BL/6JRj mice of 4-6 weeks of age obtained from Janvier laboratories. Before surgical procedures, mice were kept in groups of five, and housed in 530 cm^2 cages on a 12h light/dark cycle with unlimited access to dry food and water. Experiments were carried out during the light period. All animal experiments were performed in accordance with the German laboratory animal law guidelines for animal research and had been approved by the Landesuntersuchungsamt Rheinland Pfalz (Approval 23 177-07/G 17-1-051).

Stereotaxic injections and cranial window implantation

We followed the procedures described in detail previously [11]. Briefly, injections were performed perpendicular to the surface of the skull. Virus solution consisted of a mixture of 2 different rAAVs (rAAV8-hSyn-GCaMP6m-WPRE-hGHpolyA; titer: 1.35×10^{11} viral genomes (VG)/ml; rAAV8-hSyn-H2BmCherry-hGHpolyA; titer: 2×10^{13} VG/ml) in PBS. For another subset of experiments, rAAV8-mDlx-NLS-tagBFP-WPRE-hGHpolyA (titer: 2.16×10^{11} VG/ml) was additionally mixed with the foregoing rAAVs. 175 nL of the virus mixture loaded into a glass pipette was injected in 5 locations (20 nL/min, a total volume of 875 nL) along the anterior–posterior axis with coordinates: 4.4, −2.3/−2.6/−2.9/−3.2/−3.5, 2.5 (in mm, caudal, lateral, and ventral to Bregma) to cover the right auditory cortex. Several days after the injection, mice were anesthetized using isoflurane (maintained at 1.2-1.5 %) mounted on a stereotaxic with a custom-made v-shaped head holder. After the parietal and temporal bone was exposed, the skull above the auditory cortex (2 × 3 mm) was gently drilled and the bone was carefully lifted. The craniotomy was covered with a small cover glass, fixed with dental cement. To position the window plane perpendicular to the objective under the microscope, a custom-made titanium head post was mounted on the frontal bone and embedded with dental cement. After the surgical procedure, animals were single-housed and recovered for at least 1 week before further handling.

Habituation to awake chronic two-photon imaging

We habituated mice to handling at the 2-photon microscope. Mice were fixated under the objective in a custom-made acrylic glass tube, using a custom-made head post. The mouse head was laterally tilted such that the surface of the auditory cortex aligns with the horizontal plane. Habituation was repeated for at least 7 days, the duration of which increased from around 10 min on the first day to around 2 hours on the last day, comparable to the duration of two-photon imaging in one day.

Habituation ended when mice were accommodated to the head fixation apparatus. Since the sound stimulus set for longitudinal two-photon imaging was presented dozens of times each day, animal subjects repeatedly experienced all sound stimuli before data acquisition.

Intrinsic imaging

We identified the functional organization of auditory fields to set the location of calcium imaging within the fields via intrinsic signal imaging. We followed the protocol previously reported[46]. Briefly, the mesoscopic optical imaging was conducted using a CCD camera with macroscope objectives. Intrinsic signals were recorded from near-infrared (780 nm) LEDs while presenting pure tone pips with different tone frequencies in 30 randomized trials. The change in light reflectance between pre- and post-stimulus image was computed and averaged across trials.

Sound presentation

Sound design and delivery has been described in the previous study[11]. Briefly, all sounds were delivered free field by a ribbon loudspeaker 25 cm distance to the mouse head in a soundproof booth. The stimulus set consisted of 34 sound stimuli (19 pure-tone (PT) pips (50ms; 2 to 45 kHz separated by a quarter octave) and 15 complex sounds (CS) (70ms)) separated by one-second interval. The complex sounds were generated from arbitrary samples of music pieces or animal calls replayed at fourfold speed. All stimulus on- and offsets were smoothened by a cosine ramp function with duration of 10 msec, respectively. The stimulus set was presented 10 trials in a pseudo-random order for each field of view at 70 dB sound pressure level.

Two-photon imaging

The imaging configuration and procedure has been described in detail previously[11]. Briefly, two-photon calcium imaging was performed with a commercial microscope (Ultima IV, Bruker Corporation) with a 20×-objective (XLUMPlan Fl, NA = 0.95, Olympus) and a tunable pulsed laser (Chameleon Ultra, Coherent) in a soundproof chamber. Both GCaMP6m and mCherry were co-excited at 940 nm wavelength and separated by emission using a filter cube (U-MSWG2, Olympus). tagBFP was excited at 810 nm and separated by another filter cube (U-MWIB3). Time-series imaging was performed using a field of view (FOV) of 367 × 367 μm (pixel size: 256 × 128) at 5 Hz frame rate. In a daily session, imaging was performed not only with presentation of the sound set, but also without any sound presentation to record spontaneous neuronal activities for 144 sec in a given FOV. In the longitudinal imaging experiments, 6-8 FOVs were imaged per mouse in layer 2/3 column (about 110 – 325 μm depth from cortical surface). FOVs with reliable sound responses were repeatedly imaged at a two-day interval, except for the last imaging day (4-day interval between 6th and 7th time point). Imaging days were counted according to the day of laser ablation in ablation experiments. Z-stack images of the layer 2/3 column were also acquired in different timepoints (before starting the experiment, just before and after microablation, and after finishing the imaging experiment).

Protocol, quantification and validation of microablation

Targeted cells were identified from a full frame scan. We switched to point scan mode with dwelling time of 8 us, scan position was set at the center of nucleus of the cells. Microablation was performed with wavelength of 760 nm femtosecond laser pulses (140 fs) delivered through a 0.95 NA, 20× objective in mice that were lightly anesthetized with isoflurane (0.8-1.3%). Laser power was set between 100 – 220 mW according to the quality of fluorescence signal in the target cell. We applied the pulsed laser and immediately terminated on the detection of the abrupt elevation of Ca^{2+} fluorescence. Otherwise, we kept the laser application for up to 30 sec. If we observed clear

649 elevation of Ca^{2+} signal within a minute after laser exposure, we determined the procedure effective.
650 We took an iterative approach for ablation to increase success rate but prevent off-target damage to
651 the surrounding region at the same time (Extended Data Fig. 3a). If we did not observe such a Ca^{2+}
652 elevation, we repeated the procedure with slight increase of the laser power, at most three times. In
653 case the targeted cell still does not show any observable increase of Ca^{2+} fluorescence, we waited
654 for a few tens of minutes and again applied the laser once more. When the last application did not
655 induce an elevated Ca^{2+} signal of the cell, we categorized the cell into procedures ineffective. As
656 longer exposure times tended to produce off-target effects [48], whenever we observe abnormal Ca^{2+}
657 increase or strong bleaching in the surrounding region (approx. 50 μm in radius) during the iteration,
658 we halted the laser application and categorized the cell into procedures ineffective. In case
659 accumulated laser ablation caused massive damage to the surrounding regions (approx. >100 μm
660 in radius) of the target cells, we terminated the experiment as failure.

661 We conducted in vivo and ex vivo experiments to evaluate the microablation protocol. To keep
662 tracking cells across days in vivo, we took a single image of each FOV with size of 367×367 μm
663 (pixel size: 512 × 512) for each imaging session. We evaluated the effect of microablation by
664 taking z-stack image of layer 2/3 column including the targeted cells and comparing image of
665 nucleus and somatic fluorescence between the time points just before and after microablation, after
666 2 and 4 days, and quantifying the loss of nucleus and calcium signal for the target cells. The criteria
667 for successful ablation of the target cells are basically loss of nucleus signal in the cells described
668 as follows: a cell was identified effectively ablated when the cell demonstrated 1) complete loss
669 of nucleus fluorescence and abnormality (complete loss or excessive filling) of Ca^{2+} somatic
670 fluorescence, or 2) partial loss of nucleus signal with excessively filled Ca^{2+} fluorescence in soma.
671 On the other hand, we classified a cell as non-effectively ablated when the loss of nucleus
672 fluorescence was unclear or when the loss was partially observed but with intact Ca^{2+} somatic
673 fluorescence.

674 After 4 days of *in vivo* z-stack imaging, mice were anesthetized, the cranial windows were carefully
675 removed, and the Evans blue (Sigma-Aldrich, E2129-10G) was injected at the corners of the
676 imaged region on the cortical surface, so that the blue dye can serve as the landmark of imaged
677 region after tissue extraction. Mice were perfused with a PBS/Heparin solution and subsequently
678 with a 4% PFA solution following standard procedures. To keep the z-stack imaged volume intact
679 as much as possible, the bulk brain section over 600 μm thickness was cut roughly parallel to the
680 two-photon imaging plane on a vibratome (VT-1000, Leica Biosystems). To enable confocal
681 imaging of the bulk section, the section was cleared with the CUBIC protocol[70], washed with PBS
682 and incubated in a DAPI solution (10 μg/mL) for 24 hours. Next, Images were acquired on a
683 confocal microscope (DMi6000B CS TCS SP5, Leica) using 20x dry objective (HCX PL APO CS
684 NA=0.7) with frame size of 553.6 × 553.6 μm (pixel size: 1024 x 1024), as a z-stack with 0.5 μm
685 resolution. The region for confocal imaging was estimated by the blue-dye landmarks. By slightly
686 scaling and rotating roll, pitch, and yaw of the post-hoc 3 D confocal image, the in-vivo imaged
687 population and microablated neurons were identified in the post-hoc image data.

688 **Validation of the AAV-vector labeling inhibitory interneurons in vivo**

689 rAAV8-mDlx-NLS-tagBFP was injected into GAD67-GFP mice. After three weeks of injection,
690 the mice were deeply anesthetized with Ketamine/Medetomidine (mg/kg), perfused with 10 ml
691 PBS / Heparin and switched to 10 ml 4% PFA solution in the standard protocol. Brains were
692 extracted and sliced for every 100 μm coronal section with Vibratone (VT-1000), then mounted on
693 cover slips. Confocal images were acquired (DMi6000B CS TCS SP5) using 20x dry objective

(HCX PL APO CS). From the images, colocalization of GFP and tagBFP signals was evaluated by custom-written MATLAB scripts.

Data analysis

Image processing pipeline for chronic two-photon data

Before applying an individual cell tracking algorithm, global xy-image displacement induced by movement was corrected by cross-correlation based method[71]. Region of interests (ROIs) were semi-automatically selected by a custom-made MATLAB program, which were manually corrected later by a human expert and usually described by a set of several hundred points marking the centers of neuronal nuclei. To track individual ROIs across days, we followed a procedure described in the previous study. Generally, two-dimensional affine transformation was optimally applied to register ROIs in each frame of the time series from the same FOV across several days. Optimization of the transformation was achieved by Nelder-Mead-Simplex algorithm with MATLAB function (fminsearch), and by iterating it in the two different spatial scales which first covered the entire frame and secondly focused on the four equally split image segments to adjust local movements during two-photon scanning. Lastly, to adjust to further local distortion, individual ROIs were allowed to move up to two-pixel (2.87 μm) and find a better matching with the image.

ROI inclusion criteria and Calculation of $\Delta F/F_0$, deconvolution

To include only cells in the analysis that had a reliably present nucleus signal in the H2B:mCherry channel, we applied four quality criteria described in our previous study[11]: Nearest Neighbor Distance, Normalized Soma Signal Intensity, Soma Signal to Noise ratio and Objective Function Value, which were applied on a frame-by-frame basis, so that a cell was either reliably present or excluded at each time point. To correct fluctuating background fluorescence from somatic Ca^{2+} signal, the out-of-focus neuropil signal was calculated as the average fluorescence value of an area surrounding each individual regions of interest, and subtracted from the time series after multiplication with a contamination ratio as described before[72,73]. We calculated a contamination ratio, independently for each imaging plane in each experiment[72]. To calculate $\Delta F/F$, the baseline F_0 used to compute the $\Delta F/F_0$ was defined as a moving rank order filter, the 30th percentile of the 200 surrounding frames (100 before and 100 after). To estimate neuronal firing rate, this $\Delta F/F_0$ was then deconvolved using the conventional algorithm[74].

Stimulus-evoked sound responsiveness of single cells

To classify single cells as sound responsive or not, all the 10 trials from a given stimulus were compared in a signed-rank test against ten pre-stimulus spontaneous activity. A cell was classified as significantly responsive, if the p value was below 0.05 after a Benjamini-Hochberg (or false discovery rate, FDR) correction for multiple comparisons against number of stimuli (34), for at least one stimulus [11]. The amplitude of sound-evoked Ca^{2+} transients was calculated by subtracting the average pre-stimulus baseline $\Delta F/F$ value (2 frames corresponding -200-0 ms) from the average post-stimulus peak $\Delta F/F$ value (2 frames corresponding 200-400 ms) of all trials[72].

Analysis of spontaneous activity

From the time series of deconvolved calcium signals across neurons, we included neurons for analysis which passed through the ROI inclusion criteria for at least 30% of the recording duration (corresponding to 43 sec). In order to faithfully detect spontaneous activity, we applied a threshold equal to sum of median and median absolute deviation multiplied by scale factor k (1.483) of a series of deconvolution signals for each neuron. We detected frequency (1/sec) and amplitude of peaks in activities as spontaneous event rate and event amplitude, respectively.

FOV inclusion criteria

We included FOVs in our analysis that satisfied the following criteria: (A) FOVs needed to contain at least 100 ROIs (i.e. neurons) which fulfilled the quality criteria described above, (B) FOVs needed more than ten significantly sound responsive neurons during baseline days.

Selection of sound responsive, non-sound responsive and inhibitory cells for microablation:

During the two baseline days before microablation (day-3 and day-1), we identified sound responsive cells which showed significant sound-evoked response for at least one stimulus in each FOV. For each sound responsive cell, we calculated the average amplitude in sound responsive area which includes all the significantly responsive stimuli. We derived the amplitude distribution of responsive cells sorted in descending order for each day and created a single distribution after merging and sorting the two days distributions. In case a cell was duplicated because the cell was responsive on both the days, the higher-rank cell was selected to have unique cell identities across the merged distribution. Thus, we prepared the sorted sound-responsive distribution merged for day-3 and day-1 in each FOV, or "the distribution of candidate responsive cells". On the day of microablation, we targeted cells from the top of the distribution of candidate responsive cells.

We identified non-sound responsive cells, for each day-3 and day-1, which did not show significant response to any of sounds in each FOV, and derived the amplitude distributions of these cells sorted by absolute amplitude in ascending order. We selected the cells responsive on neither of the days, which equal to the cells existing in both the distributions. We calculated the average rankings of the cells from both the distributions and sorted again the cells based on the average ranking in ascending order to prepare "the distribution of candidate non-responsive cells". On the day of microablation, we targeted cells from the highest rank (i.e., smallest absolute amplitude) of candidate non-responsive cells.

For inhibitory cell ablation group, we included the sound-responsive inhibitory interneurons based on the same criteria for the sound responsive ablation. To achieve comparable number of cells to be microablated to the other groups of ablation experiment, we also included interneurons with non-significant but large transient amplitude after sound presentation (apparent sound responsive cells), in case the number of sound responsive cells does not reach the prerequisite number for each FOV. These apparent sound responsive cells were also sorted based on their amplitude averaged across the 2 days, then we selected cells from the highest amplitudes. Practically in the experiment of microablation of sound responsive, non-responsive or inhibitory responsive cells, we had to avoid cells for microablation when the cells showed unclear nucleus fluorescence due to optical occlusion by blood vessels, weak expression, out-of-focus position. In the end we were able to target 4-8 cells for microablation in each FOV.

In the control group, on the day when the animals would have undergone microablation in ablation experiments, mice (N = 7) were set in the microscope chamber under the comparable level of isoflurane anesthesia (~3 hours) without any additional laser application except for monitoring Ca^{2+} and nucleus fluorescence for tens of minutes. Another 2 mice were set in the microscope chamber, but only for short anesthetic exposure (~half an hour) to acquire a few z stack images of the FOVs. Our offline analysis confirmed that the control mice exposed to long isoflurane anesthesia on day 0 and the other control mice with short isoflurane exposure on day 0 did not show any distinct difference in average best response amplitude across neurons on day +1 (baseline-normalized amplitude for long anesthetic exposure: 1.072 ± 0.086; for short anesthetic exposure: 1.063 ± 0.047; two-sample t-test, $p = 0.96$) nor fraction of responsiveness on day +1 (baseline-normalized fraction

782 for long anesthetic exposure: 0.915 ± 0.057; for short anesthetic exposure: 1.114 ± 0.088; two-
783 sample t-test, p = 0.085).

784 **Exclusion of cells with unsuccessful ablation and cells nearby ablated cells**

785 Targeted cells include all the cells to which we applied the laser for ablation. For any microablation
786 experiment, a small proportion of the targeted cells showed unclear effect of ablation, based on the
787 criteria we described above. Since some of unclearly ablated cells also demonstrated abnormal Ca^{2+}
788 signals such as lower frequency of Ca^{2+} transients than before, or seizure-like bursting behavior,
789 we excluded all the targeted cells and nearby cells for further analysis. Following a previous study[33],
790 we excluded targeted neurons (regardless of whether microablation was successful or not), as well
791 as neurons within a sphere centered on ablated neurons having a radius of 15 μm, from any analysis.

792 **Definition of high and low category cells**

793 In addition, to make a fair comparison between different ablation experiments, we digitally filtered
794 out highly sound responsive cells and/or non-sound responsive cells from spared population as
795 'filtered condition' for further analysis. To mimic response property and number of the ablated non-
796 responsive cells in non-responsive ablation group, we defined five non-responsive cells with
797 minimum absolute amplitudes per FOV in sound responsive ablation group, which we would have
798 ablated in non-responsive ablation experiment (we call these non-responsive cells, which were
799 supposed to be physically or digitally excluded, "low category cells"). Conversely, to mimic
800 response property and number of the ablated sound responsive cells in sound responsive ablation
801 group, we defined five responsive cells with highest amplitudes per FOV in non-responsive
802 ablation group (we call these responsive cells "high category cells"). Then, we digitally excluded
803 low category cells from the spared population in sound responsive ablation group, high category
804 cells in non-responsive ablation group, and both low and high category cells in control group,
805 respectively. We verified that the number of ablated sound responsive cells and other high category
806 cells were comparable between groups (Extended Fig. 4e), that the number of ablated non-
807 responsive cells and other low category cells were also comparable (Extended Fig. 4f). We also
808 confirmed that the best response amplitudes of high category cells had no significant difference
809 between groups (Extended Fig. 4h), the response amplitude of low category cells was not
810 significantly different (Extended Fig. 4i) and the number of spared cells in the filtered condition
811 were comparable between the different ablation groups (Extended Fig. 4j).

812 **Single-cell tuning correlation**

813 For a given sound responsive cell, the trials were pseudo-randomly split into two sets with the half
814 number of trials. Response amplitudes along the 34 stimuli were averaged across each half of the
815 trials. Then Pearson correlation of the averaged responses was calculated between the first and the
816 second half set of trials. This procedure was repeated 10 times, and we averaged these correlation
817 values as single-cell tuning correlation for each day. To evaluate correlation to day-1, instead of
818 calculating Pearson correlation of the averaged responses of half trials on the same day, we
819 calculated correlation between the averaged response of half trials on day-1 and the averaged
820 response of half trials on the other day.

821 **Representational map**

822 Pearson correlation of sound-evoked response vector among cells in each FOV to different stimuli
823 was calculated for each trial and averaged across trials for each day[10]. Then, a similarity matrix
824 was constructed where each element in the matrix corresponds to trial-averaged correlation
825 coefficient for each combination of stimuli, excluding pairs with the same trials. Note that each

diagonal element, trial-averaged correlation to the same stimulus corresponds to the trial-by-trial reliability of population response to each stimulus. Representational map was generated by averaging all the similarity matrices across all the FOVs in each group of mice for each day. A dimension-reduced representational map was also formed by applying Principal component analysis (PCA), where a similarity matrix was mapped onto 2-dimensional (1st and 2nd) eigenvector space. Each data point in the space represents principal component scores of the correlation profile in the similarity matrix corresponding to one of the 34 standard stimuli.

Decoding

A support vector machine a with linear kernel was trained to discriminate each pair of stimuli from the 34 stimuli as a binary classifier, using a built-in function in MATLAB, fitcecoc. In either case that training and testing was done on the same day, or done on different days, cross-validation was performed by 5-fold cross validation. Training and testing the classifier was conducted for a population in each FOV. The decoding performance was defined as the percentage of correctly classified trials, which was averaged across FOVs per mouse and averaged across mice for each experimental group.

Statistical analysis

All statistical analyses were performed using MATLAB (Mathworks, Natick, MA, USA). Most statistical comparisons were performed using One-way ANOVA to test changes across imaging days for each experimental group, and afterward the two-sided paired t-test comparing paired means within individual mice for two different conditions like different days, day -3 and day +1. For comparison between different experimental cohorts in a given day or in a set of days, the two-sided t-test was applied after false discovery rate (FDR) correction for multiple comparison. In all cases, we treated not neurons but mice as independent observations. When classifying individual neurons for sound-evoked responsiveness, since post-stimulus activities across trials were highly non-normally distributed, a signed-rank test was performed after Benjamini-Hochberg correction for multiple comparisons against number of stimuli. For the same reason, to compare the normalized correlation coefficient in the representational maps across the experimental cohorts (Extended Data Fig. 5 and 9), we used a non-parametric pairwise multiple comparisons, Dunn's test for the different pairs of cumulative distribution of the normalized correlation coefficient, as well as Mann-Whitney U test after FDR correction to compare medians between the cohorts for each tested day. Sample sizes were largely comparable between conditions (number of mice between the different cohorts). No statistical tests were applied to determine sample sizes.

References

1 Gregory, S. *et al.* Operationalizing compensation over time in neurodegenerative disease. *Brain* **140**, 1158-1165, doi:10.1093/brain/awx022 (2017).

2 Stern, Y., Barnes, C. A., Grady, C., Jones, R. N. & Raz, N. Brain reserve, cognitive reserve, compensation, and maintenance: operationalization, validity, and mechanisms of cognitive resilience. *Neurobiol. Aging* **83**, 124-129, doi:10.1016/j.neurobiolaging.2019.03.022 (2019).

3 Haxby, J. V. *et al.* Distributed and Overlapping Representations of Faces and Objects in Ventral Temporal Cortex. *Science* **293**, 2425–2430 (2001).

4 Kriegeskorte, N. *et al.* Matching categorical object representations in inferior temporal cortex of man and monkey. *Neuron* **60**, 1126-1141, doi:10.1016/j.neuron.2008.10.043 (2008).

5 Kriegeskorte, N., Mur, M. & Bandettini, P. Representational similarity analysis - connecting the branches of systems neuroscience. *Front. Syst. Neurosci.* **2**, 4, doi:10.3389/neuro.06.004.2008 (2008).

6 Niessing, J. & Friedrich, R. W. Olfactory pattern classification by discrete neuronal network states. *Nature* **465**, 47-52, doi:10.1038/nature08961 (2010).

7 Pashkovski, S. L. *et al.* Structure and flexibility in cortical representations of odour space. *Nature* **583**, 253-258, doi:10.1038/s41586-020-2451-1 (2020).

8 Deitch, D., Rubin, A. & Ziv, Y. Representational drift in the mouse visual cortex. *Current biology : CB* **31**, 4327-4339 e4326, doi:10.1016/j.cub.2021.07.062 (2021).

9 Low, I. I. C., Williams, A. H., Campbell, M. G., Linderman, S. W. & Giocomo, L. M. Dynamic and reversible remapping of network representations in an unchanging environment. *Neuron* **109**, 2967-2980 e2911, doi:10.1016/j.neuron.2021.07.005 (2021).

10 Bathellier, B., Ushakova, L. & Rumpel, S. Discrete neocortical dynamics predict behavioral categorization of sounds. *Neuron* **76**, 435-449, doi:10.1016/j.neuron.2012.07.008 (2012).

11 Aschauer, D. F. *et al.* Learning-induced biases in the ongoing dynamics of sensory representations predict stimulus generalization. *Cell reports* **38**, 110340, doi:https://doi.org/10.1016/j.celrep.2022.110340 (2022).

12 Ziv, Y. *et al.* Long-term dynamics of CA1 hippocampal place codes. *Nat. Neurosci.* **16**, 264-266, doi:10.1038/nn.3329 (2013).

13 Driscoll, L. N., Pettit, N. L., Minderer, M., Chettih, S. N. & Harvey, C. D. Dynamic Reorganization of Neuronal Activity Patterns in Parietal Cortex. *Cell* **170**, 986-999 e916, doi:10.1016/j.cell.2017.07.021 (2017).

14 Schoonover, C. E., Ohashi, S. N., Axel, R. & Fink, A. J. P. Representational drift in primary olfactory cortex. *Nature* **594**, 541-546, doi:10.1038/s41586-021-03628-7 (2021).

15 Yasumatsu, N., Matsuzaki, M., Miyazaki, T., Noguchi, J. & Kasai, H. Principles of long-term dynamics of dendritic spines. *The Journal of neuroscience : the official journal of the Society for Neuroscience* **28**, 13592-13608, doi:10.1523/JNEUROSCI.0603-08.2008 (2008).

16 Xu, T. *et al.* Rapid formation and selective stabilization of synapses for enduring motor memories. *Nature* **462**, 915-919, doi:10.1038/nature08389 (2009).

17 Cane, M., Maco, B., Knott, G. & Holtmaat, A. The relationship between PSD-95 clustering and spine stability in vivo. *The Journal of neuroscience : the official journal of the Society for Neuroscience* **34**, 2075-2086, doi:10.1523/JNEUROSCI.3353-13.2014 (2014).

18 Loewenstein, Y., Yanover, U. & Rumpel, S. Predicting the Dynamics of Network Connectivity in the Neocortex. *The Journal of neuroscience : the official journal of the Society for Neuroscience* **35**, 12535-12544, doi:10.1523/JNEUROSCI.2917-14.2015 (2015).

19 Melander, J. B. *et al.* Distinct in vivo dynamics of excitatory synapses onto cortical pyramidal neurons and parvalbumin-positive interneurons. *Cell reports* **37**, 109972, doi:10.1016/j.celrep.2021.109972 (2021).

20 Kasai, H., Ziv, N. E., Okazaki, H., Yagishita, S. & Toyoizumi, T. Spine dynamics in the brain, mental disorders and artificial neural networks. *Nat Rev Neurosci* **22**, 407-422, doi:10.1038/s41583-021-00467-3 (2021).

21 Ziv, N. E. & Brenner, N. Synaptic Tenacity or Lack Thereof: Spontaneous Remodeling of Synapses. *Trends Neurosci.* **41**, 89-99, doi:10.1016/j.tins.2017.12.003 (2018).

22 Loewenstein, Y., Kuras, A. & Rumpel, S. Multiplicative dynamics underlie the emergence of the log-normal distribution of spine sizes in the neocortex in vivo. *The Journal of neuroscience : the official journal of the Society for Neuroscience* **31**, 9481-9488, doi:10.1523/JNEUROSCI.6130-10.2011 (2011).
23 Burianova, J., Ouda, L. & Syka, J. The influence of aging on the number of neurons and levels of non-phosporylated neurofilament proteins in the central auditory system of rats. *Front. Aging Neurosci.* **7**, 27, doi:10.3389/fnagi.2015.00027 (2015).
24 Merrill, D. A., Chiba, A. A. & Tuszynski, M. H. Conservation of neuronal number and size in the entorhinal cortex of behaviorally characterized aged rats. *The Journal of comparative neurology* **438**, 445-456, doi:10.1002/cne.1327 (2001).
25 Stranahan, A. M., Jiam, N. T., Spiegel, A. M. & Gallagher, M. Aging reduces total neuron number in the dorsal component of the rodent prefrontal cortex. *The Journal of comparative neurology* **520**, 1318-1326, doi:10.1002/cne.22790 (2012).
26 Yates, M. A., Markham, J. A., Anderson, S. E., Morris, J. R. & Juraska, J. M. Regional variability in age-related loss of neurons from the primary visual cortex and medial prefrontal cortex of male and female rats. *Brain Res.* **1218**, 1-12, doi:10.1016/j.brainres.2008.04.055 (2008).
27 Elman, J. A. *et al.* Neural compensation in older people with brain amyloid-beta deposition. *Nat. Neurosci.* **17**, 1316-1318, doi:10.1038/nn.3806 (2014).
28 Mongillo, G., Rumpel, S. & Loewenstein, Y. Inhibitory connectivity defines the realm of excitatory plasticity. *Nat. Neurosci.* **21**, 1463-1470, doi:10.1038/s41593-018-0226-x (2018).
29 Chen, G., Kang, B., Lindsey, J., Druckmann, S. & Li, N. Modularity and robustness of frontal cortical networks. *Cell* **184**, 3717-3730 e3724, doi:10.1016/j.cell.2021.05.026 (2021).
30 Li, N., Daie, K., Svoboda, K. & Druckmann, S. Robust neuronal dynamics in premotor cortex during motor planning. *Nature* **532**, 459-464, doi:10.1038/nature17643 (2016).
31 Houweling, A. R. & Brecht, M. Behavioural report of single neuron stimulation in somatosensory cortex. *Nature* **451**, 65-68 (2008).
32 Buchan, M. J. & Rowland, J. M. Stimulation of Individual Neurons Is Sufficient to Influence Sensory-Guided Decision-Making. *The Journal of neuroscience : the official journal of the Society for Neuroscience* **38**, 6609-6611, doi:10.1523/JNEUROSCI.1026-18.2018 (2018).
33 Peron, S. *et al.* Recurrent interactions in local cortical circuits. *Nature* **579**, 256-259, doi:10.1038/s41586-020-2062-x (2020).
34 Robinson, N. T. M. *et al.* Targeted Activation of Hippocampal Place Cells Drives Memory-Guided Spatial Behavior. *Cell* **183**, 1586-1599 e1510, doi:10.1016/j.cell.2020.09.061 (2020).
35 Cannon, W. B. & Rosenberg, C. E. *The wisdom of the body*. (W.W. Norton & Company, Inc, 1932).
36 Turrigiano, G. G., Leslie, K. R., Desai, N. S., Rutherford, L. C. & Nelson, S. B. Activity-dependent scaling of quantal amplitude in neocortical neurons. *Nature* **391** (1998).
37 Turrigiano, G. G. & Nelson, S. B. Homeostatic plasticity in the developing nervous system. *Nat Rev Neurosci* **5**, 97-107, doi:10.1038/nrn1327 (2004).
38 Turrigiano, G. G. The self-tuning neuron: synaptic scaling of excitatory synapses. *Cell* **135**, 422-435, doi:10.1016/j.cell.2008.10.008 (2008).
39 Marder, E. & Goaillard, J. M. Variability, compensation and homeostasis in neuron and network function. *Nat Rev Neurosci* **7**, 563-574, doi:10.1038/nrn1949 (2006).
40 Davis, G. W. Homeostatic control of neural activity: from phenomenology to molecular design. *Annual review of neuroscience* **29**, 307-323, doi:10.1146/annurev.neuro.28.061604.135751 (2006).
41 Styr, B. & Slutsky, I. Imbalance between firing homeostasis and synaptic plasticity drives early-phase Alzheimer's disease. *Nat. Neurosci.* **21**, 463-473, doi:10.1038/s41593-018-0080-x (2018).
42 Slomowitz, E. *et al.* Interplay between population firing stability and single neuron dynamics in hippocampal networks. *Elife* **4**, doi:10.7554/eLife.04378 (2015).
43 Chen, T. W. *et al.* Ultrasensitive fluorescent proteins for imaging neuronal activity. *Nature* **499**, 295-300, doi:10.1038/nature12354 (2013).
44 Nathanson, J. L., Yanagawa, Y., Obata, K. & Callaway, E. M. Preferential labeling of inhibitory and excitatory cortical neurons by endogenous tropism of adeno-associated virus and lentivirus vectors. *Neuroscience* **161**, 441-450, doi:10.1016/j.neuroscience.2009.03.032 (2009).

45 Kato, H. K., Gillet, S. N. & Isaacson, J. S. Flexible Sensory Representations in Auditory Cortex Driven by Behavioral Relevance. *Neuron* **88**, 1027-1039, doi:10.1016/j.neuron.2015.10.024 (2015).

46 Chambers, A. R., Aschauer, D. F., Eppler, J. B., Kaschube, M. & Rumpel, S. A stable sensory map emerges from a dynamic equilibrium of neurons with unstable tuning properties. *Cereb. Cortex* **33**, 5597-5612, doi:10.1093/cercor/bhac445 (2022).

47 Fu, Y. *et al.* A cortical circuit for gain control by behavioral state. *Cell* **156**, 1139-1152, doi:10.1016/j.cell.2014.01.050 (2014).

48 Vladimirov, N. *et al.* Brain-wide circuit interrogation at the cellular level guided by online analysis of neuronal function. *Nat. Methods* **15**, 1117-1125, doi:10.1038/s41592-018-0221-x (2018).

49 Wu, G. K., Arbuckle, R., Liu, B. H., Tao, H. W. & Zhang, L. I. Lateral sharpening of cortical frequency tuning by approximately balanced inhibition. *Neuron* **58**, 132-143, doi:10.1016/j.neuron.2008.01.035 (2008).

50 Kato, H. K., Asinof, S. K. & Isaacson, J. S. Network-Level Control of Frequency Tuning in Auditory Cortex. *Neuron* **95**, 412-423 e414, doi:10.1016/j.neuron.2017.06.019 (2017).

51 Lakunina, A. A., Nardoci, M. B., Ahmadian, Y. & Jaramillo, S. Somatostatin-Expressing Interneurons in the Auditory Cortex Mediate Sustained Suppression by Spectral Surround. *The Journal of neuroscience : the official journal of the Society for Neuroscience* **40**, 3564-3575, doi:10.1523/JNEUROSCI.1735-19.2020 (2020).

52 Marks, T. D. & Goard, M. J. Stimulus-dependent representational drift in primary visual cortex. *Nat Commun* **12**, 5169, doi:10.1038/s41467-021-25436-3 (2021).

53 Khatib, D. *et al.* Experience, not time, determines representational drift in the hippocampus. *bioRxiv* **08.31.506041**, doi:10.1101/2022.08.31.506041 (2022).

54 Chambers, A. R. & Rumpel, S. A stable brain from unstable components: Emerging concepts and implications for neural computation. *Neuroscience* **357**, 172-184, doi:10.1016/j.neuroscience.2017.06.005 (2017).

55 Rule, M. E. & O'Leary, T. Self-healing codes: How stable neural populations can track continually reconfiguring neural representations. *Proceedings of the National Academy of Sciences of the United States of America* **119**, doi:10.1073/pnas.2106692119 (2022).

56 Kossio, Y. F. K., Goedeke, S., Klos, C. & Memmesheimer, R. M. Drifting assemblies for persistent memory: Neuron transitions and unsupervised compensation. *Proceedings of the National Academy of Sciences of the United States of America* **118**, doi:10.1073/pnas.2023832118 (2021).

57 Hill, R. A., Damisah, E. C., Chen, F., Kwan, A. C. & Grutzendler, J. Targeted two-photon chemical apoptotic ablation of defined cell types in vivo. *Nat Commun* **8**, 15837, doi:10.1038/ncomms15837 (2017).

58 London, M., Roth, A., Beeren, L., Hausser, M. & Latham, P. E. Sensitivity to perturbations in vivo implies high noise and suggests rate coding in cortex. *Nature* **466**, 123-127, doi:10.1038/nature09086 (2010).

59 Turrigiano, G. Homeostatic synaptic plasticity: local and global mechanisms for stabilizing neuronal function. *Cold Spring Harb. Perspect. Biol.* **4**, a005736, doi:10.1101/cshperspect.a005736 (2012).

60 Chen, L., Li, X., Tjia, M. & Thapliyal, S. Homeostatic plasticity and excitation-inhibition balance: The good, the bad, and the ugly. *Current opinion in neurobiology* **75**, 102553, doi:10.1016/j.conb.2022.102553 (2022).

61 Barnes, S. J. *et al.* Subnetwork-Specific Homeostatic Plasticity in Mouse Visual Cortex In Vivo. *Neuron* **86**, 1290-1303, doi:10.1016/j.neuron.2015.05.010 (2015).

62 Kilman, V., van Rossum, M. C. W. & Turrigiano, G. G. Activity Deprivation Reduces Miniature IPSC Amplitude by Decreasing the Number of Postsynaptic GABA A Receptors Clustered at Neocortical Synapses. *The Journal of neuroscience : the official journal of the Society for Neuroscience* **22**, 10 (2002).

63 Vale, C. & Sanes, D. H. The effect of bilateral deafness on excitatory and inhibitory synaptic strength in the inferior colliculus. *The European journal of neuroscience* **16**, 2394-2404, doi:10.1046/j.1460-9568.2002.02302.x (2002).

64 Hartman, K. N., Pal, S. K., Burrone, J. & Murthy, V. N. Activity-dependent regulation of inhibitory synaptic transmission in hippocampal neurons. *Nat. Neurosci.* **9**, 642-649, doi:10.1038/nn1677 (2006).

65 Keck, T. *et al.* Loss of Sensory Input Causes Rapid Structural Changes of Inhibitory Neurons in Adult Mouse Visual Cortex. *Neuron* **71**, 869-882, doi:10.1016/j.neuron.2011.06.034 (2011).

66 Takesian, A. E., Kotak, V. C., Sharma, N. & Sanes, D. H. Hearing loss differentially affects thalamic drive to two cortical interneuron subtypes. *Journal of neurophysiology* **110**, 999-1008, doi:10.1152/jn.00182.2013 (2013).

67 Resnik, J. & Polley, D. B. Fast-spiking GABA circuit dynamics in the auditory cortex predict recovery of sensory processing following peripheral nerve damage. *Elife* **6**, doi:10.7554/eLife.21452 (2017).

68 Gainey, M. A. & Feldman, D. E. Multiple shared mechanisms for homeostatic plasticity in rodent somatosensory and visual cortex. *Philosophical transactions of the Royal Society of London. Series B, Biological sciences* **372**, doi:10.1098/rstb.2016.0157 (2017).

69 Chan, Y. C. *et al.* An unbiased AAV-STARR-seq screen revealing the enhancer activity map of genomic regions in the mouse brain in vivo. *Sci. Rep.* **13**, 6745, doi:10.1038/s41598-023-33448-w (2023).

70 Tainaka, K. *et al.* Whole-Body Imaging with Single-Cell Resolution by Tissue Decolorization. *Cell* **159**, 911-924, doi:10.1016/j.cell.2014.10.034 (2014).

71 Miri, A., Daie, K., Burdine, R. D., Aksay, E. & Tank, D. W. Regression-based identification of behavior-encoding neurons during large-scale optical imaging of neural activity at cellular resolution. *Journal of neurophysiology* **105**, 964-980, doi:10.1152/jn.00702.2010 (2011).

72 Tischbirek, C. H. *et al.* In Vivo Functional Mapping of a Cortical Column at Single-Neuron Resolution. *Cell reports* **27**, 1319-1326 e1315, doi:10.1016/j.celrep.2019.04.007 (2019).

73 Kerlin, A. M., Andermann, M. L., Berezovskii, V. K. & Reid, R. C. Broadly tuned response properties of diverse inhibitory neuron subtypes in mouse visual cortex. *Neuron* **67**, 858-871, doi:10.1016/j.neuron.2010.08.002 (2010).

74 Vogelstein, J. T. *et al.* Fast nonnegative deconvolution for spike train inference from population calcium imaging. *Journal of neurophysiology* **104**, 3691-3704, doi:10.1152/jn.01073.2009 (2010).

75 Ouellet, L. & de Villers-Sidani, E. Trajectory of the main GABAergic interneuron populations from early development to old age in the rat primary auditory cortex. *Front. Neuroanat.* **8**, 40, doi:10.3389/fnana.2014.00040 (2014).

76 Kwan, A. C., Dietz, S. B., Zhong, G., Harris-Warrick, R. M. & Webb, W. W. Spatiotemporal dynamics of rhythmic spinal interneurons measured with two-photon calcium imaging and coherence analysis. *Journal of neurophysiology* **104**, 3323-3333, doi:10.1152/jn.00679.2010 (2010).

1063 **Figure Legends**

1064

1065 **Fig. 1** Chronic in vivo two-photon imaging of sound-evoked population responses.

1066 **a.** Schematic of the experiment for longitudinal Ca^{2+} imaging in the mouse auditory cortex. **b.**
1067 Example imaging plane showing broad expression of GCaMP6m and H2B::mCherry in layer 2/3
1068 neurons. **c.** Exemplary responses to auditory stimuli (19 pure tones ranging between 2 - 45 kHz
1069 and 15 complex sounds) of the neurons indicated in b. **d.** Normalized response profiles for each
1070 imaging day for the subset of neurons categorized as sound responsive on day -1. **e.** Normalized
1071 correlation of single-trial stimulus tuning between day-1 and the other day, for the neurons shown
1072 in d. **f.** Same as d, however, considering the neurons that were categorized as sound responsive on
1073 each given day. **g.** Same as e, but single-trial correlation for each day. **h.** Similarity matrix of
1074 population response vectors for all stimuli averaged across all FOVs for each day. **i.** Correlations
1075 averaged across diagonal elements (dark green) and off-diagonal elements (light green) in the
1076 similarity matrices shown in h normalized to baseline (day -5 to day -1). **j.** Display of the
1077 representational map generated by the projection of the similarity matrices shown onto the 1st and
1078 2nd principal component using PCA. Each color dot represents one of the 34 sound stimuli in PC
1079 space. **k.** Correlation matrix of population vectors across all the imaging days. The correlation
1080 across all stimulus pairs was averaged for each matrix element.

1081

1082 **Fig. 2** Probing the robustness of a representational map by microablation of functionally
1083 characterized neurons.

1084 **a.** Representative example of two-photon microablation of a functionally characterized cell with
1085 pure tone tuning. Upper inset: Before ablation, Lower inset: 2 days after ablation. Microablated
1086 cells showed permanent loss of nucleus signal and sound-evoked signal. Scale: 50 μm. **b.**
1087 Specificity of single-cell ablation protocol. **c.** Target cells for microablation. Top: Sorted sound-
1088 evoked amplitudes on day -1 in a FOV. For the group of sound responsive microablation, 5 - 8 cells
1089 of highly responsive cells were targeted per FOV, in 6 - 8 FOVs per mouse in a layer 2/3 column.
1090 For the non-sound responsive microablation group, a similar number of non-responsive cells were
1091 targeted. Control group had no microablation on day 0. Experimentally targeted or corresponding
1092 responsive and non-responsive cells were excluded and further data analysis was conducted on
1093 remaining spared cells (gray bars in bottom inset). **d.** Similarity matrix of population vectors for
1094 all stimuli averaged across all FOVs for each day in sound responsive microablation cohort,
1095 analogous to Fig. 1 h. **e.** Baseline-normalized correlations averaged across diagonal elements (dark
1096 orange) and off-diagonal elements (light orange) in the similarity matrices in d. **f.** Dimension-
1097 reduced display of the representational map from each similarity matrix shown in d. **g.** Correlation
1098 matrix of population vectors across all the imaging days. **h.** Same as d, but similarity matrix in non-
1099 sound responsive ablation condition. **i.** Same as e, but baseline-normalized correlations averaged
1100 across diagonal elements (dark blue) and off-diagonal elements (light blue) in the similarity
1101 matrices in h. **j.** Same as f, but dimension-reduced representational map from each similarity matrix
1102 in h. **k.** Same as g, but correlation matrix of population vectors between days in non-sound
1103 responsive ablation condition.

1104

1105

Fig. 3 Changes in response properties of individual neurons after microablation.

a. Fraction of sound-responsive cells over the imaging days (mean ± s.e.m. across mice. Orange, blue, and green lines indicate sound responsive ablation, non-sound responsive ablation and control group, respectively). **b.** Averaged tuning curves of cells showing significant responses to pure-tones (left) or complex sound stimuli (right) normalized to the maximal response (mean ± s.e.m.) for day-1 and day +5. Stimuli are aligned and sorted by response magnitude for each cell individually. **c.** Baseline-normalized best response amplitude of cells responsive for each day. Best response amplitude is the response amplitude of the stimulus evoking the largest significant response. **d.** Baseline-normalized fraction of cells categorized as sound responsive on a given imaging day, but also on the subsequent imaging day, providing a measure of tuning stability. **e.** Same as Fig. 1d, but normalized response profiles of neurons with a significant response on day -1 in sound responsive ablation condition. **f.** Same as Fig. 1 e, but normalized correlation of single-trial stimulus tuning between day -1 and the other day, of individual neurons responsive on day -1 in sound responsive ablation (orange) and in control (green) conditions. **g.** Same as Fig. 2 e, but normalized response profiles in non-sound responsive ablation. **h.** Same as Fig. 2 f, but normalized correlation of single-trial stimulus tuning between day -1 and the other day, in non-sound responsive ablation (blue) and in control (green) conditions. **i.** Exemplary sound-evoked Ca^{2+} transients of neurons which respond to sounds on day -1 but reduce the amplitudes in the following days after ablation in sound responsive ablation (left), non-sound responsive ablation (middle), and control (right), respectively. Left inset indicates the sound which elicited the response, and insets next to Ca^{2+} transients show images of cell on different days. **j.** Exemplary sound-evoked Ca^{2+} transients of neurons unresponsive on day -1, but becoming responsive in the following days after ablation. **k.** Top: Scheme of splitting neurons into two groups based on their responsiveness on day -1. Bottom: Baseline-normalized best response amplitude for cells responsive on day-1 (left) and for cells not responsive on day -1 but responsive on the other day (right) plotted across days (mean ± s.e.m. across mice. Orange, blue, and green line indicate sound responsive ablation, non-sound responsive ablation and control group, respectively). **l.** Left: Scheme of signal correlation between microablated cells and spared cells, pairs of which are defined based on the responsiveness on day -1 and day +i. Right: Colormaps show baseline-subtracted fraction of cells with signal correlation between microablated cells (or high category cells except for sound responsive ablation group) and spared cells, which are responsive on day -1 (top) and not responsive on day -1 but responsive on the other day (bottom). Bar plots next to the colormap are fractions of cells for signal correlation bins averaged across baseline days (day -5 and day -3) in each split group.

Fig. 4 Excitatory and inhibitory neurons are differentially affected after microablation.

a. Field of view showing broad expression of GCaMP6m and H2B::mCherry (left) and selective expression of tagBFP in interneurons (right), of mouse auditory cortex. Scale: 100 µm. **b.** Averaged tuning curves of cells responsive to pure-tones (top) or complex sound stimuli (bottom) normalized to the maximal response for excitatory (Exc: red line) and inhibitory neurons (Inh: blue line) during a baseline day in control condition. **c.** Same as Fig. 3d, but normalized fraction of neurons responsive on both days for excitatory (left) and inhibitory (right) neurons, in the three experimental conditions. Data presented as mean ± s.e.m. across mice (5 mice for sound responsive ablation; 5 mice for non-sound responsive ablation; 7 mice for control). **d.** Same as Fig. 3f, but normalized correlation of single-trial stimulus tuning between day -1 and the other day for excitatory (left) and inhibitory (right) neurons. **e.** Representative excitatory (top left) and inhibitory (bottom left) neurons, which change response amplitude to sound stimuli from day -1 to day +5, in sound responsive ablation. Right: Baseline-normalized best response across days for excitatory (red) and inhibitory (blue) neurons. **f.** Baseline-normalized E-I ratio between average best responses of excitatory and inhibitory neurons. Data presented as mean ± s.e.m. across mice.

Fig. 5 Selective microablation of inhibitory neurons.

a. Target cells for inhibitory-cell microablation. Top: Sorted sound-evoked amplitudes on day -1 in a FOV, where interneurons are labeled as blue bars and putative excitatory cells as gray bars. Middle: Sorted amplitudes of the same population above but only from interneurons. 5 - 8 cells of highly responsive interneurons were targeted per FOV. **b.** Representative example of microablation of a targeted inhibitory cell with PT & CS tuning. Scale: 20 µm. **c.** Same as Fig. 2 d, but similarity matrix of population vectors to the sound stimuli, averaged across all FOVs for each day in inhibitory cell ablation condition. **d.** Same as Fig. 2e, but baseline-normalized average correlation in diagonal (dark pink) and off-diagonal (light pink) elements of the similarity matrices in c. **e.** Same as Fig. 2f, but dimension-reduced representational map from each similarity matrix in c. **f.** Same as Fig. 2g, but correlation matrix of population vectors across all the imaging days in inhibitory cell ablation condition. **g-l.** Same as Fig. 3a-f, but for inhibitory cell ablation condition, respectively. **m.** Same as Fig. 3k, but baseline-normalized best response amplitude for cells responsive on day -1 (left) and for cells not responsive on day -1 but responsive on the other day (right) plotted across days in inhibitory cell ablation condition. **n.** Same as Fig. 3l, but baseline-subtracted fraction of cells with signal correlation between high category cells and spared cells in inhibitory cell ablation condition.

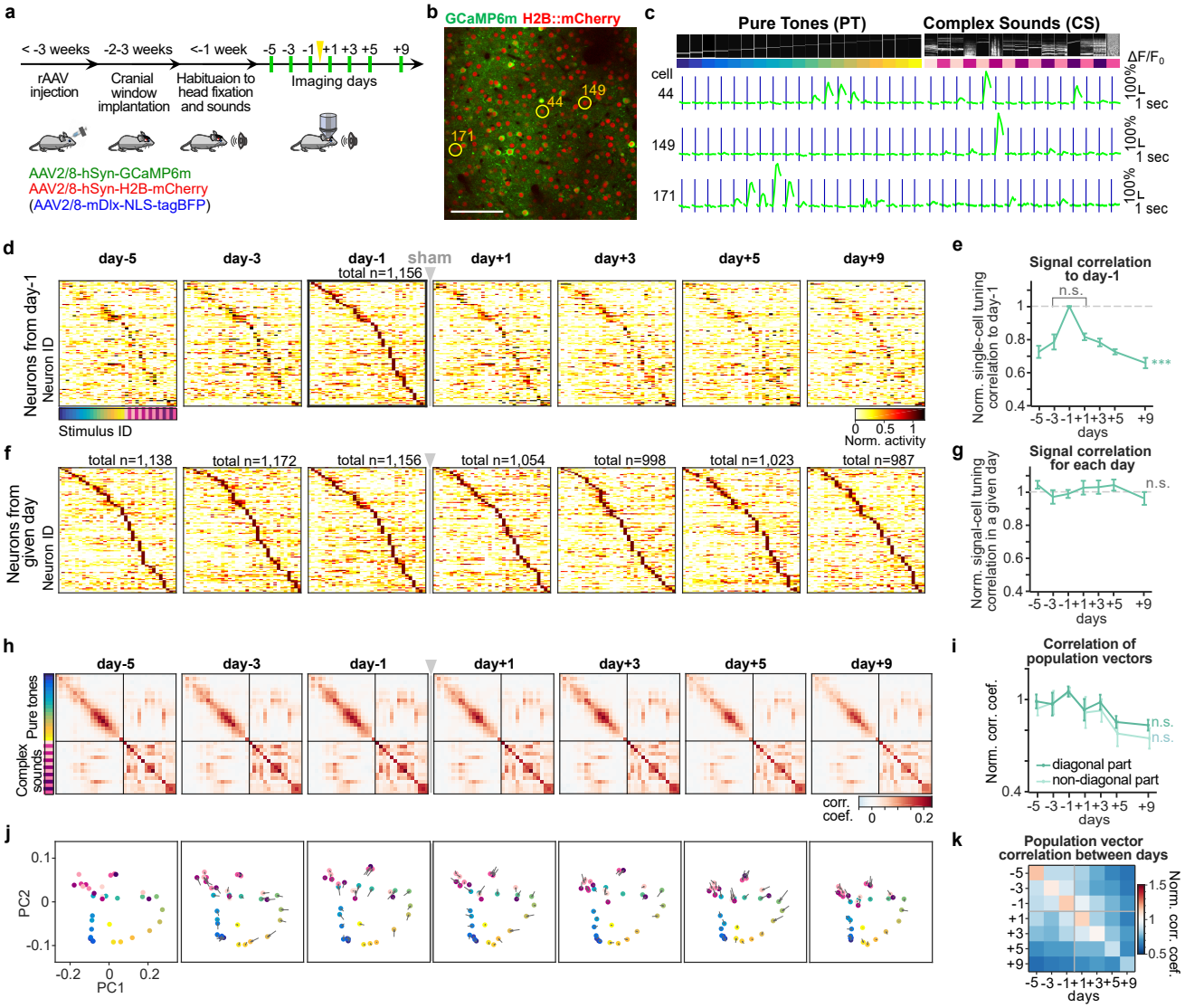

Fig. 1 Chronic in vivo two-photon imaging of sound-evoked population responses

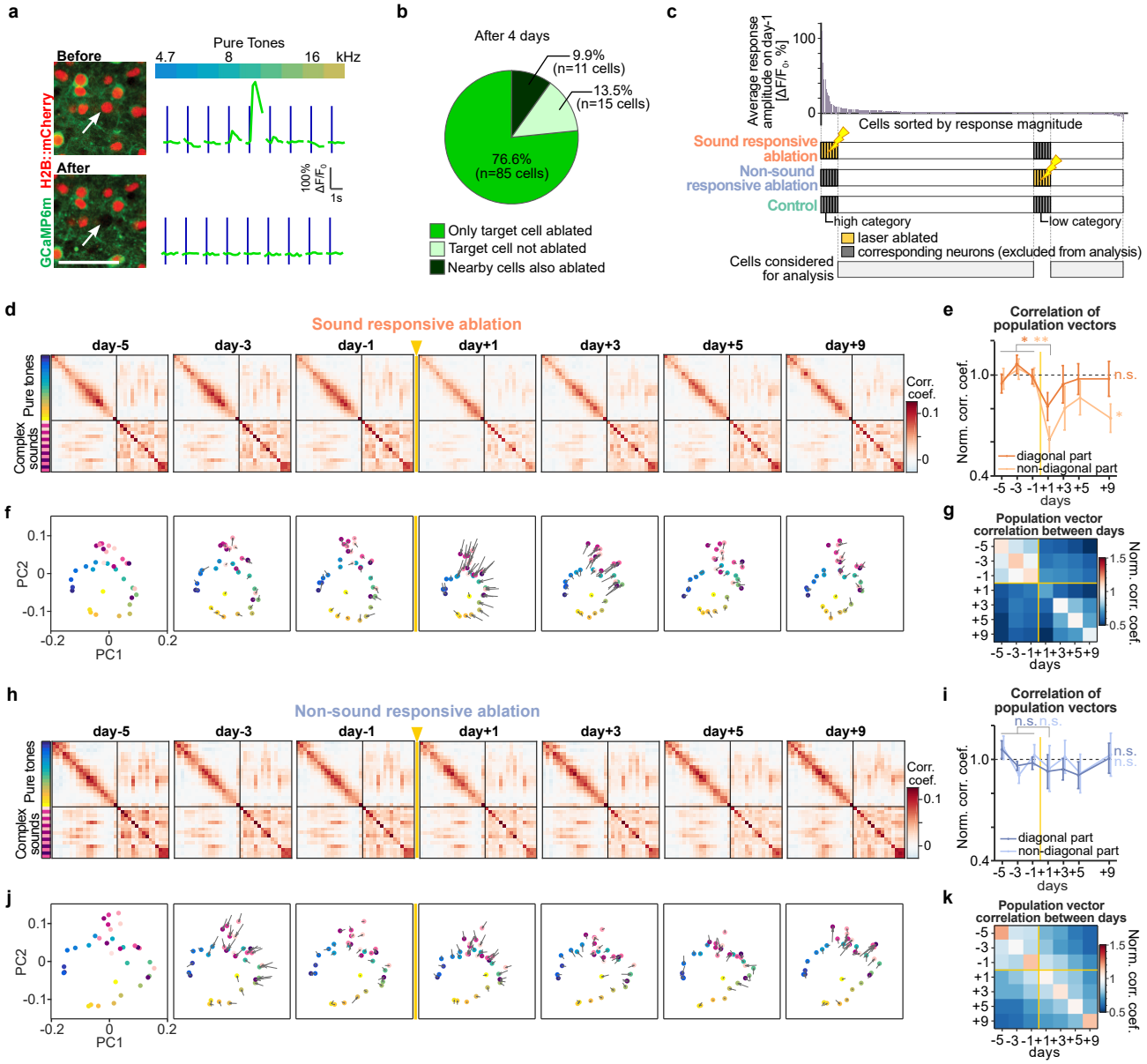

Fig. 2 Probing the robustness of a representational map by microablation of functionally characterized neurons

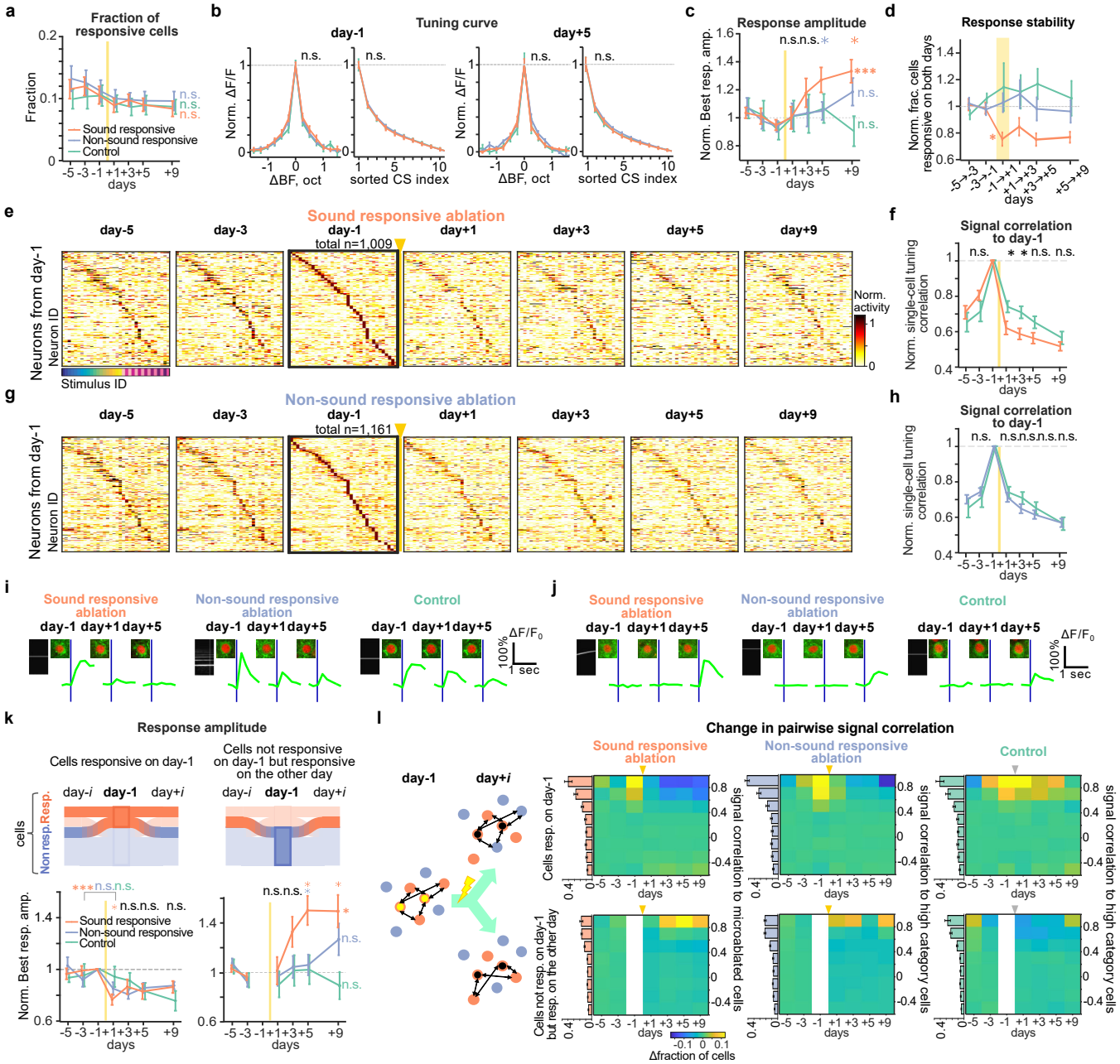

Fig. 3 Changes in response properties of individual neurons after microablation

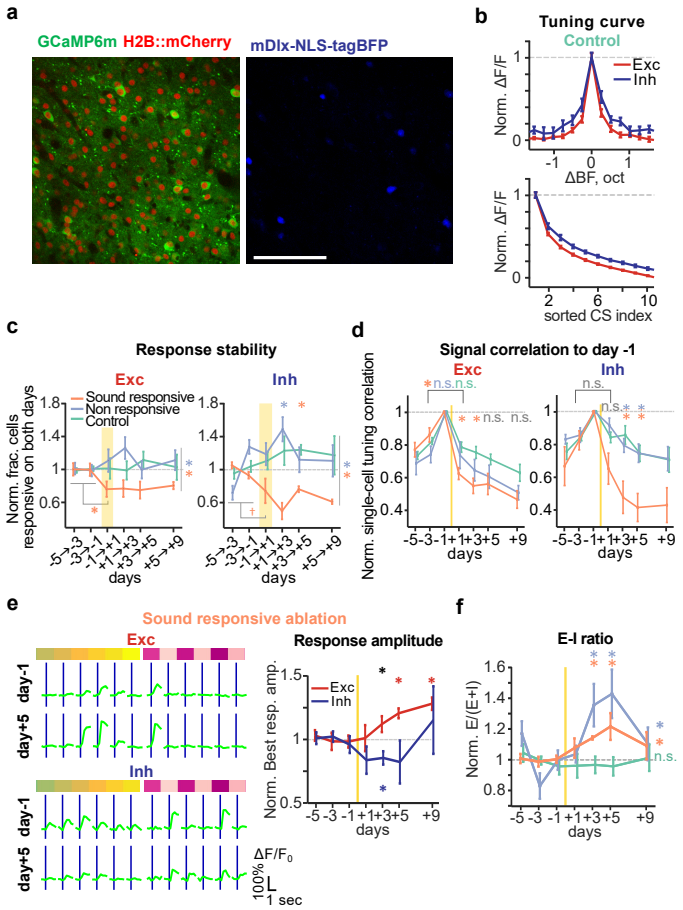

Fig. 4 Excitatory and inhibitory neurons are differentially affected after microablation

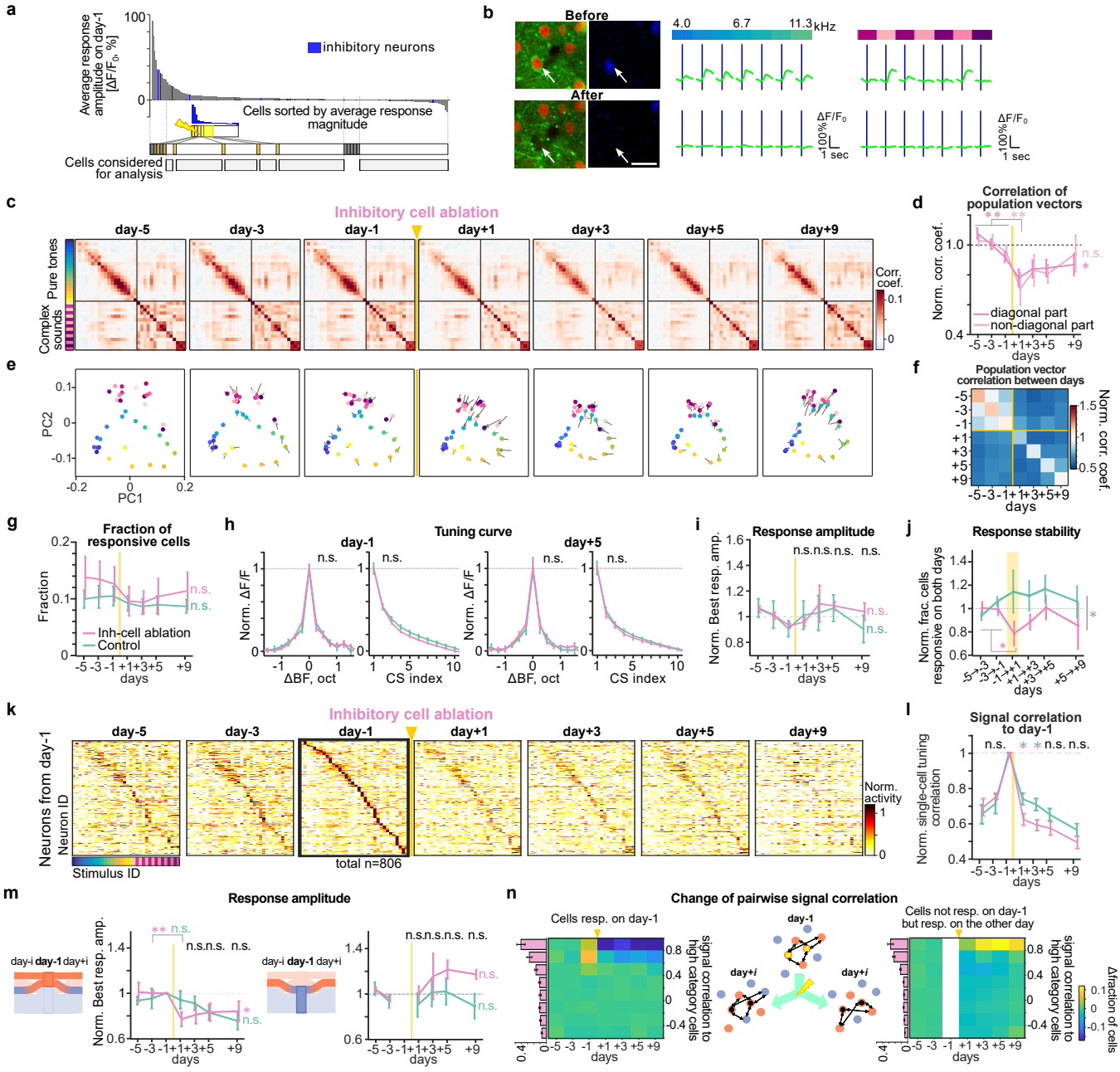

Fig. 5 Selective microablation of inhibitory neurons